J. Fluid Mech. (2010), *vol.* 653, *pp.* 431–462.
doi:10.1017/S0022112010000406

Near-wall estimates of the concentration and orientation distribution of a semi-dilute rigid fibre suspension in Poiseuille flow

P. J. KROCHAK[1]†, J. A. OLSON[1] AND D. M. MARTINEZ[2]

[1]Department of Mechanical Engineering, University of British Columbia, 2054-6250 Applied Science Lane, Vancouver, BC, V6T 1Z4, Canada

[2]Department of Chemical and Biological Engineering, University of British Columbia, 2360 East Mall, Vancouver, BC, V6T 1Z4, Canada

(Received 15 June 2009; revised 20 January 2010; accepted 20 January 2010; first published online 30 April 2010)

A model is presented to predict the orientation and concentration state of a semi-dilute, rigid fibre suspension in a plane channel flow. A probability distribution function is used to describe the local orientation and concentration states of the suspension and evolves according to a Fokker–Planck equation. The fibres are free to interact with each other hydrodynamically and are modelled using the approach outlined by Folgar & Tucker (*J. Reinf. Plast. Comp.* vol. 3, 1984, p. 98). Near the channel walls, the no-flux boundary conditions as proposed by Schiek & Shaqfeh (*J. Fluid Mech.* vol. 296, 1995, p. 271) are applied on the orientation distribution function. With this approach, geometric constraints are used to couple the fibres' rotary motion with their translational motion. This eliminates physically unrealistic orientation states in the near-wall region. The concentration distribution is modelled in a similar manner to that proposed by Ma & Graham (*Phys. Fluids* vol. 17, 2005, art. 083103). A two-way coupling between the fibre orientation state and the momentum equations of the suspending fluid is considered. Experiments are performed to validate the numerical model by visualizing the motion of tracer fibres in an index-of-refraction matched suspension. The orientation distribution function is determined experimentally based on these observations of fibre motion and a comparison is made with the model predictions. Good agreement is shown particularly near the channel walls. The results indicate that at distances less than one-half of a fibre length from the channel walls, the model accurately predicts the available fibre orientation states and the distribution of fibres amongst these states. The model further predicts a large concentration gradient in this region that is also observed experimentally. The magnitude of the concentration gradient in the near-wall region is shown to increase with increasing fibre concentration.

1. Introduction

In this work, we study the near-wall behaviour of rigid non-Brownian fibre suspensions flowing through a rectangular channel; see figure 1. The case considered here is for flow with semi-dilute suspensions consisting of rigid rods suspended in a viscous, Newtonian fluid. Here, semi-dilute is defined such that $1 \leqslant nL^3 \leqslant r$, where

† Email address for correspondence: krochak@interchange.ubc.ca

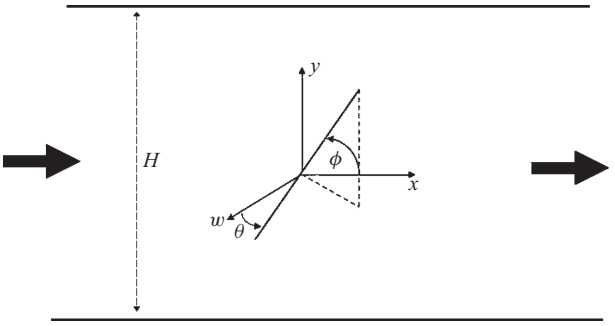

FIGURE 1. The channel geometry and fibre orientation angles used in this study. The large arrows indicate the direction of the flow.

n is the number of fibres per unit volume, L is the fibre length and r is the fibre aspect ratio, that is, the ratio of fibre length to its diameter. The Reynolds number considered here based on the length of the fibre is asymptotically small.

Fibre suspension flows play an important role in many industrial processes. During processing, fibre orientation can determine the quality of the final products, for example in paper-making, composite materials manufacturing and the electrospinning of nano-fibres. It has also been established that the transport, suspension rheology and flow field respond to the orientation and concentration state of the suspension (e.g. Batchelor 1970; Cox 1970; VerWeyst & Tucker 2002; Lipscomb & Denn 1988). It is widely known that fibres suspended in a fluid undergo mean motion because of the fluid velocity and random motions due to hydrodynamic fibre–fibre interactions.

Early theoretical developments in fibre suspension rheology have shown that the rotary motion of a single, freely suspended fibre in a moving fluid depends entirely on the local velocity gradients in the flow. Jeffery (1922) was the first to formally prove this relationship. By using a no-slip boundary condition along the surface of a fibre and matching the velocity field in the region near the fibre to the bulk flow field of the suspending medium, Jeffery derived an expression for the angular velocity of an isolated fibre. His derivation showed that a single fibre will rotate continuously in one of an infinite set of closed orbits around the vorticity axis. Bretherton (1962) advanced the argument that Jeffery's equations apply to cylindrical particles if the particle aspect ratio r is replaced by an effective aspect ratio. This was confirmed experimentally by Goldsmith & Mason (1962).

Jeffery's classic analysis is limited to the infinitely dilute case. As the fibre concentration increases, deviations are observed from Jeffery's predictions. The discrepancy stems from the fact that fibres interact hydrodynamically with neighbouring fibres at distances on the order of a fibre length. Folgar & Tucker (1984) addressed this issue by modelling hydrodynamic fibre–fibre interactions as a diffusional process and defined an empirically determined rotary diffusion coefficient D_r. They proposed, through a simple dimensional analysis, a relationship in which D_r is linearly proportional to the magnitude of the rate of strain tensor $\|\boldsymbol{E}\|$

$$D_r = C_I \|\boldsymbol{E}\|, \tag{1.1}$$

where C_I is traditionally called the interaction coefficient and is related to suspension parameters such as concentration, aspect ratio and fibre length. It should be noted that (1.1) implies isotropic diffusion. Ranganathan & Advani (1991) challenged the utility of this approach. They used the Folgar–Tucker model to relate the interaction

coefficient, C_I, to the average interparticle spacing in non-dilute suspensions. They found a strong dependence between C_I and the orientation state of the suspension. Specifically, by fitting the experimental data of Folgar (1983) for $nL^3 = 52.2$, they found that C_I was an order of magnitude larger when the suspension was in an isotropic orientation state compared to that in an aligned orientation state. This phenomenon however was not found to be significant when $nL^3 = 26$. What these studies did show was an orientation state dependence of the interaction coefficient at higher concentrations. The findings of Ranganathan & Advani (1991) spurred the derivation of more complex models for the rotary diffusion coefficient; see for example Koch (1995) or Phelps & Tucker (2009). While these models have the potential to improve the accuracy of fibre orientation estimates, they are computationally more intensive due to the introduction of higher-order orientation tensors. Furthermore, these models require additional closure parameters whose values are not typically available *a priori*.

In a similar manner, hydrodynamic fibre–fibre interactions cause deviations to the translational motion of fibres (e.g. Kim 1986; Stover 1991). Here, the interactions create disturbances that seemingly mimic a diffusional process. Rahnama *et al.* (1993) derived an expression for the hydrodynamic translational diffusion in dilute suspensions by computing an ensemble average of two-body interactions. While two-body interactions apply only to dilute suspensions, they were able to extend the dilute relationship to the semi-dilute regime by accounting for hydrodynamic screening, i.e. a reduction in the spatial range through which fibre–fibre interactions propagate throughout the suspension. Using the experimental data of Anczurowski & Mason (1968), they derived the following expression for the translational diffusion coefficient in the wall-normal direction:

$$D_t = 1.7 \times 10^{-2} \frac{nL^3L^2}{r \ln \zeta/a} \|\boldsymbol{E}\|, \tag{1.2}$$

where a is the fibre radius and ζ is defined in terms of the fibre volume fraction, c, as $\zeta = (nL)^{1/2} \ln^{1/2}(1/c)$). The key finding of this work is that D_t should increase with increasing fibre concentration.

It is well understood that the local flow field plays a fundamental role in determining the motion of suspended fibres. However, the flow of fibre suspensions differs considerably from the flow of a pure fluid. The earliest reports of this were made by Forgacs, Robertson & Mason (1958). They showed that the flow of semi-dilute fibre suspensions can be classified by one of three distinct regimes depending on the velocity of the suspension. At very low velocity, they report a plug-flow with no movement of fibres relative to one another and a thin water layer near the walls. Furthermore, velocity gradients were only found to exist within this water layer. At higher velocities, they report that the wall layer becomes unstable and a turbulent annulus forms that begins to break up the plug. They termed this the mixed flow regime. At high velocity, the flow becomes fully turbulent and the fibre network breaks up leaving turbulent flow across the entire channel. In a more recent study, Xu & Aidun (2005) measured velocity profiles arising from the flow of semi-dilute fibre suspensions through a rectangular channel using pulsed ultrasound Doppler velocimetry (PUDV). They varied both the fibre concentration and the Reynolds number and determined the effect of each on the flow profile. At low Reynolds number, they showed that as the fibre concentration increased, the velocity profile changes from a parabolic to a plug-type velocity distribution. The size of the plug region was also found to increase

with fibre concentration. When in this state, they argued that the fibres form an 'interlocking coherent network' in the central part of the channel with a thin liquid layer between the plug and the wall. This fibre network was believed to increase the momentum transfer between the fluid and fibre phase. A similar phenomenon was observed by Heath *et al.* (2007), who experimentally studied the flow of a 0.4 % mass concentration pulp suspension through an axisymmetric 1:5 sudden expansion. They found that for a mean velocity, $U \approx 0.5\,\mathrm{m\,s^{-1}}$, the suspension moved as a plug far beyond the expansion with a plug-like concentration distribution. Velocity profiles were also measured and showed a similar, plug-like velocity distribution. At higher velocities, specifically when $0.7\,\mathrm{m\,s^{-1}} \leqslant U \leqslant 0.9\,\mathrm{m\,s^{-1}}$, concentration profile measurements showed that the plug region had been fluidized, and a more uniform concentration distribution was observed. However, PUDV measurements revealed that the suspension flowed with a plug-like velocity distribution despite having a more even spatial distribution of the fibres.

It is also understood that suspension flows are coupled to the orientation state through its rheology. The first to address this issue theoretically was Batchelor (1970), who developed a general constitutive equation for the bulk stress in a suspension of rigid, inertialess particles of arbitrary shape in a Newtonian fluid. By representing a single particle in suspension as a distribution of Stokeslets over a line enclosed by the particle body, Batchelor determined expressions for the resultant force required to sustain translational motion and the resultant couple required to sustain rotational motion. Dinh & Armstrong (1984) extended Batchelor's theory to account for the orientation state of elongated particles and its effect on the bulk stress within the suspension. This was accomplished by assuming that the orientation state of the suspension can be completely described by a known orientation distribution function, ψ, such that the probability of finding fibres oriented between the angles ϕ and $\phi + \partial\phi$ is $\psi(\phi)\partial\phi$. By linearizing the flow field around the particle they were able to equate Batchelor's constitutive equation to a new constitutive equation: one that is proportional to the fourth-order moment tensor of ψ. The proportionality constant is referred to as the effective viscosity of the suspension. Bibbo, Dinh & Armstrong (1985) validated the work of Dinh & Armstrong (1984) by experimentally measuring the shear stress within a semi-concentrated suspension undergoing a simple shear flow. Their measurements demonstrated a strong coupling between fibre alignment and the resulting shear stress within the suspension and that the Dinh–Armstrong model was suitable for predicting the additional fibre stress. Using numerical techniques, Mackaplow & Shaqfeh (1996) derived expressions for the effective viscosity of dilute and semi-dilute suspensions of rods in a Newtonian fluid. For semi-dilute fibre suspensions, they express the fibre stress as follows:

$$\boldsymbol{\tau}^{fibre} = \mu^f \boldsymbol{E} : (\langle \boldsymbol{pppp} \rangle - \boldsymbol{I} \langle \boldsymbol{pp} \rangle), \tag{1.3}$$

where $\langle \boldsymbol{pppp} \rangle$ and $\langle \boldsymbol{pp} \rangle$ are the fourth- and second-order moments of the orientation distribution function ψ with respect to the orientation vector $\boldsymbol{p}$. These are often referred to as the fourth- and second-order orientation tensors, respectively, and are defined as

$$\langle \boldsymbol{pppp} \rangle = \int p_i p_j p_k p_l \psi \, \mathrm{d}\boldsymbol{p}, \quad \langle \boldsymbol{pp} \rangle = \int p_i p_j \psi \, \mathrm{d}\boldsymbol{p}, \tag{1.4}$$

where $\boldsymbol{p}$ is a unit vector pointing in the direction parallel to the axis of the fibre, that is

$$\boldsymbol{p} = \begin{bmatrix} \cos\phi \sin\theta \\ \sin\phi \sin\theta \\ \cos\theta \end{bmatrix}, \tag{1.5}$$

where ϕ is the projected angle of the fibre in the xy-plane and θ is the angle between the fibre and the z-axis; see figure 1. In (1.3), $\boldsymbol{I}$ is the unit tensor and μ^f is the effective viscosity of the suspending fluid defined as

$$\frac{\mu^f}{\mu} = \frac{\pi n L^3}{6\ln(2r)} Q(\epsilon) + A \frac{\pi n^2 L^6}{3\ln^3(2r)}, \tag{1.6}$$

where μ is the Newtonian fluid viscosity, $\epsilon = 1/\ln(2r)$ and $Q(\epsilon)$ is an $O(\epsilon^2)$ correction factor, which Batchelor (1971) defined for circular cylinders as follows:

$$Q(\epsilon) = \frac{1 + 0.64\epsilon}{1 - 1.5\epsilon} + 1.659\epsilon^2. \tag{1.7}$$

Finally, A in (1.6) is a constant that depends on the orientation state of the suspension. For an isotropic orientation distribution, $A_{iso} = 0.222$, whereas for an aligned suspension, $A_{al} = 0.206$.

The second- and fourth-order orientation tensors, $\langle \boldsymbol{pp} \rangle$ and $\langle \boldsymbol{pppp} \rangle$, can be computed using one of two general descriptions of fibre orientation, namely the Eulerian and the Lagrangian methods. With the Lagrangian method, the equations of motion are solved for each fibre in the suspension for a given velocity field. Upon computing a statistically significant number of fibre trajectories, an orientation distribution function can be determined from which $\langle \boldsymbol{pp} \rangle$ and $\langle \boldsymbol{pppp} \rangle$ can be computed. The Lagrangian method can be quite accurate, however it is computationally intensive, particularly for non-dilute suspensions. For example, Gillissen *et al.* (2007) showed that the computational time required to gain a statistically significant number of fibre trajectories using the Lagrangian method in conjunction with a direct numerical simulation of the fluid flow at a Reynolds number of $Re = 360$ would be in excess of 100 years on a 2 GHz processor. With the Eulerian description, the suspension is treated as a continuous phase and the position and orientation of the fibres are described by a probability density function. The main advantage of the Eulerian method is that it is computationally more efficient than particle-level simulations and can easily handle the complex fibre–fibre interactions and the two-way coupling between the flow field and the fibre orientation state. However, the Eulerian method does have a number of shortcomings. Specifically, the Eulerian method is unable to model accurately mechanical interactions of the fibres, either with walls or with other fibres in the suspension. Another issue is that the Eulerian method cannot describe the detailed motion of any individual fibre. For example, it is common to find real fibres in a so-called flipping state, i.e. fibres that rotate continuously by 180° about their centre. However, only a small $O(1/r)$ fraction of the fibres will be found in a flipping state at any given time (Rahnama, Koch & Shaqfeh 1995*b*). As a result, resolving such detailed phenomena will not improve significantly the description of the fibre suspension but will add an enormous computational cost. In fact, the Eulerian method is able to predict the state of a suspension adequately for most engineering applications. With the Eulerian description, the probability density of fibres having orientation $\boldsymbol{p}$ and position $\boldsymbol{r}$ at time t is denoted as $\Psi(\boldsymbol{r}, \boldsymbol{p}, t)$. The convection-diffusion model that governs the

evolution of Ψ is given by, e.g. Olson *et al.* (2004),

$$\frac{\partial \Psi}{\partial t} = D_r \nabla_r^2 \Psi - \nabla_r \cdot (\boldsymbol{\omega} \Psi) + D_t \nabla^2 \Psi - \nabla \cdot (\boldsymbol{V} \Psi), \tag{1.8}$$

where $\boldsymbol{V}$ is the mean translational velocity of the fibres, $\boldsymbol{\omega}$ is the fibres angular velocity and ∇_r is the rotational operator expressed as

$$\nabla_r = \boldsymbol{p} \times \frac{\partial}{\partial \boldsymbol{p}}. \tag{1.9}$$

The angular velocity of the fibre, $\boldsymbol{\omega}$, is related to the fibres rotational vector by the following expression:

$$\boldsymbol{\omega} = \boldsymbol{p} \times \dot{\boldsymbol{p}}. \tag{1.10}$$

A number of research groups often neglect both the translational diffusivity and the translational velocity of the fibres and assume that fibres are uniformly distributed throughout the domain and translate strictly along streamlines (e.g. Leal & Hinch 1971; Folgar & Tucker 1984; Altan *et al.* 1989; Koch 1995; Lin & Zhang 2002; Parsheh, Brown & Aidun 2005). This simplification is well justified for unbounded flows, or when computing Ψ far enough away from channel walls. However, this simplification can lead to inaccuracies near solid walls. To highlight this, if $0 < D_t \ll 1$, to leading order the model cannot resolve the behaviour near solid boundaries as the highest-order derivative has been neglected.

Neglecting the fibres cross-streamline translational velocity can also lead to erroneous results, particularly near walls. For example, Leighton & Acrivos (1987) demonstrate a curious phenomenon where the effective viscosity of a concentrated suspension of neutrally buoyant, non-Brownian spheres decreases over time when subject to a constant strain rate. They showed that this drift in the effective viscosity was the result of particles migrating out of the shearing planes and into a reservoir containing the stagnant part of the suspension. Associated with this particle migration was a decrease in particle concentration in the shearing planes. They argued that particle migration stems from an irreversible hydrodynamic coupling between the particles and the fluid, which leads to particle migration from regions of high to low shear stress. Phillips *et al.* (1992) extended the work of Leighton & Acrivos (1987) by deriving a constitutive equation for the shear-induced migration of spherical particles in concentrated suspensions. Their model includes the effect of spatially varying particle–particle interactions and the effect of spatially varying viscosity. They show that the particle–particle interactions scale with the local strain rate, while the viscosity-induced migration scales with the variation of the local effective viscosity. This model was coupled to the fluid flow equations and estimates were made of both the concentration distribution and velocity profile in a Couette flow. Their predictions were shown to agree very well with experimental measurements of the particle concentration in a Couette flow device. Specifically, the particle concentration was found to be lowest in the near-wall region and increased monotonically to a maximum value near the central core of the flow.

A similar phenomenon is also known to occur with the flow of orientable polymer suspensions. In this case, polymers have been observed to migrate away from walls resulting in a so-called depletion zone (e.g. Agarwal, Dutta & Mashelkar 1994 and the references therein). As with non-Brownian particles, one of the key mechanisms responsible for polymer migration is believed to be a strong coupling between the local polymer concentration, effective viscosity and the velocity field, i.e. hydrodynamic interactions between particles and fluid. With this in mind, Ma & Graham (2005)

derived an expression for the centre-of-mass migration velocity of orientable polymer molecules normal to the wall. Using a bead–spring dumbbell model for the polymer, they showed that to leading order, the migration velocity v_{mig} is estimated as

$$v_{mig} = \frac{3}{64\pi\mu n}\left(\frac{N_1(y) - N_2(y)}{y^2} + \frac{N_1(H-y) - N_2(H-y)}{(H-y)^2}\right), \tag{1.11}$$

where y is the perpendicular distance from the wall, and N_1 and N_2 are the first and second normal polymer stress differences defined as

$$N_1 = \tau^f_{xx} - \tau^f_{yy}, \qquad N_2 = \tau^f_{yy} - \tau^f_{zz}. \tag{1.12}$$

An evolution equation governing the centre-of-mass probability distribution, i.e. the local 'concentration' distribution, $n(\boldsymbol{r}, t)$, can be extracted from (1.8) by integrating (1.8) over $\boldsymbol{p}$, enforcing periodic boundary conditions in Ψ, i.e. $\partial\Psi/(\partial\phi_{\phi=-\pi/2}) = \partial\Psi/(\partial\phi_{\phi=\pi/2})$ and defining

$$\Psi(\boldsymbol{r}, \boldsymbol{p}, t) = n(\boldsymbol{r}, t)\psi(\boldsymbol{r}, \boldsymbol{p}, t), \tag{1.13}$$

$$n(\boldsymbol{r}, t) = \int \Psi(\boldsymbol{r}, \boldsymbol{p}, t)\mathrm{d}\boldsymbol{p}. \tag{1.14}$$

This results in the following governing equation for the centre-of-mass probability distribution, $n(\boldsymbol{r}, t)$:

$$\frac{\partial n}{\partial t} = \nabla \cdot (D_t \nabla n - \boldsymbol{V}\, n) \tag{1.15}$$

subject to the no-flux boundary condition at the channel walls, i.e.

$$D_t \nabla n - \boldsymbol{V}\, n = 0. \tag{1.16}$$

Experimental evidence has demonstrated that the rotational behaviour of orientable particles is quite different near solid boundaries compared with its behaviour in central parts of a channel. Stover & Cohen (1990) appear to be the first to rigorously address this issue experimentally. In their studies, the motion of rodlike particles in a low-Reynolds-number plane Poiseuille flow was observed experimentally and the effect of the wall on the period of fibre rotation was determined. They found that when particles with a high Jeffery orbit constant, that is particles with a large period of rotation about the vorticity axis, came within a distance less than half a fibre length from the wall, an irreversible interaction between the fibre and the wall occurred where the fibre was said to 'pole-vault' away from the wall to a distance of approximately half a fibre length. This interaction was named accordingly as it seemingly mimicked the flipping motion of a pole-vaulter. Yet, the fibre was said to never actually touch the wall but rather that the fibre tip would come within approximately one fibre diameter from the wall. They suggested the existence of some non-hydrodynamic force between the fibre and the wall but could not determine the exact nature of this interaction. They observed quite a different behaviour for fibres with a low Jeffery orbit constant that came within a half-fibre length from the wall. In this case, the fibre remained close to the wall indefinitely. If the fibre had a period of rotation somewhere between these extremes, it shifted its orientation away from the wall. In studies by Moses, Advani & Reinhardt (2001), the rotational and translational motion of a single fibre near a solid boundary was measured experimentally in simple shear. These studies showed that for locations less than a fibre length from the wall, fibres rotate to position themselves parallel to the wall and remain in this orientation

indefinitely. They concluded that for these fibres, the wall has a stabilizing effect on the fibre.

Capturing the unique, near-wall behaviour of fibre suspensions using an Eulerian description is not a trivial matter. The simplest, and most easily satisfied wall boundary condition for ψ is a simple no-flux condition, i.e. fibres, and hence ψ cannot be carried through solid walls. This condition is naturally satisfied by the no-slip and no-penetration conditions for the fluid along a wall. Furthermore, it is both sensible and straightforward to apply this condition to spherical particles. However, for elongated, orientable particles, the no-flux condition is not so simple. For example, if the centre of a fibre is positioned at a distance less than half of its length away from a wall, the fibre is not free to assume all possible orientations since some configurations would place one end of the fibre inside the wall. This suggests the existence of a set of forbidden orientation states, i.e. those orientations that are non-physical. The basis for this condition lies in the impenetrability of a rigid particle through a solid wall. **?** present a general framework for the construction of the near-wall boundary conditions based on the impenetrability condition. These rigorous boundary conditions were later implemented by Schiek & Shaqfeh (1995) to study the flow of non-dilute, Brownian suspensions. It was shown that the surface over which the zero-flux boundary condition must be satisfied is not simply that of the wall, but rather a complex hypersurface that forbids any part of the fibre from penetrating the wall. Explicitly, the near-wall boundary conditions can be expressed as follows:

$$\boldsymbol{n} \cdot (\boldsymbol{j}_r + \boldsymbol{j}_t) = 0 \tag{1.17}$$

where $\boldsymbol{n}$ is the local, unit normal to the hypersurface separating the allowed and forbidden fibre orientation states. $\boldsymbol{j}_r$ and $\boldsymbol{j}_t$ are respectively the rotational and translational fluxes of the probability density function, ψ, i.e.

$$\boldsymbol{j}_t = D_t \nabla \psi - (\boldsymbol{V}\ \psi), \tag{1.18}$$

$$\boldsymbol{j}_r = D_r \nabla_r \psi - (\boldsymbol{\omega}\ \psi). \tag{1.19}$$

In words, (1.17) states that any rotational flux that places one end of the fibre into the wall must be balanced by a translation flux that moves the centre of the fibre away from the wall. It should be pointed out, however, that these boundary conditions alone do not necessarily include hydrodynamic interactions with the wall, but rather consider the steric depletion of allowable orientation states only. Using a non-local theory for the polymer stress and the rigorous no-flux boundary conditions described above, Schiek & Shaqfeh (1995) show that Ψ changes rapidly over the length of a fibre as it approaches the wall. In their calculations, the rotary Péclet number, that is the ratio of strain rate to rotary diffusion, was of order 1. This rapid variation in Ψ implies that fibres experience a rapid variation in the concentration field and in the Brownian force and torque in this near-wall region. They showed a near-linear increase in the concentration distribution with small deviations as the Péclet number increased. Nitsche & Roy (1996) used the rigorous near-wall boundary conditions on Ψ along with hydrodynamic wall interactions to investigate relationships between wall effects and configurational distributions of Brownian suspensions at small Péclet numbers. Independent calculations were performed using a bead–spring dumbbell model, and for spheroid-type particle, solutions were obtained using a perturbation expansion with respect to the Péclet number. They concluded that steric effects of the wall act to impede shear-induced alignment while hydrodynamic wall interactions increase angular variation through an effective increase in the local rotary Péclet

number. They further showed that higher-order terms in the perturbation expansion create deviations in the orientation and concentration distributions, similar to those showed by Schiek & Shaqfeh (1995).

In recent years, there has been a redeveloped interest in fibre suspension flows in relationship to turbulent drag reduction. For example, the numerical predictions of Paschkewitz *et al.* (2004) show that turbulent drag could be reduced by as much as 26 % when non-Brownian fibres are added to a flow. Their numerical simulations further showed that the mechanism responsible for these reductions in drag stems from near-wall interactions between the fibre and fluid phases. More specifically, it was concluded that velocity fluctuations in the wall-normal direction are reduced, while streamwise fluctuations and vorticity are simultaneously increased. These findings would suggest that the near-wall interactions between the fluid and fibre phases is critical to the turbulent drag reduction phenomenon.

This paper investigates the translational and rotational behaviours of rigid, non-Brownian fibres near solid walls in Poisieulle flow. To do so, we use the rigorous formulation of the no-flux boundary conditions described by Schiek & Shaqfeh (1995) to constrain fibre orientation near the channel walls along with the hydrodynamic fibre–wall interaction model described by Ma & Graham (2005) to predict fibre migration in the wall-normal direction. A comparison is made between numerical estimates of the local orientation and concentration distributions with experimental measurements at three different concentrations, i.e. $nL^3 = 3.6$, $nL^3 = 10.8$ and $nL^3 = 15.0$. The model is then used to predict the velocity profiles arising from the fibre suspension flow through a rectangular channel, and these calculations are then compared to the experimental results of Xu & Aidun (2005). In § 2, we formulate the numerical model along with a derivation of the boundary conditions as they apply to this particular flow. In § 3, we measure the orientation distribution of tracer fibres in an index-of-refraction matched solution of rigid glass rods suspended in a viscous Newtonian fluid as a function of distance across the channel. The results of this study along with a discussion thereof are given in § 4.

2. Problem formulation

In this section, the model equations are presented and applied specifically to the rectangular channel shown in figure 1. The following assumptions are made in the analysis outlined below:

(*a*) The fibres are assumed to be neutrally buoyant.

(*b*) Hydrodynamic fibre–fibre interactions are assumed to result in an isotropic rotational diffusivity as modelled by (1.1). This relationship for D_r is applied to the entire flow domain and is assumed to be unmodified close to the walls.

(*c*) The translational motion of the fibres normal to the flow direction is assumed to be the result of shear-induced migration and random motions resulting from hydrodynamic fibre–fibre interactions.

(*d*) Flow through the channel is assumed to be two-dimensional and a planar model of fibre orientation is considered where each fibre is assumed to be oriented in the xy-plane with an orientation described by the single angle ϕ. With this assumption, the fibre orientation vector in the xy-plane is defined as follows:

$$\boldsymbol{p} = \begin{bmatrix} \cos\phi \\ \sin\phi \end{bmatrix}. \tag{2.1}$$

(*e*) The flow field is coupled to the fibre phase through (1.3) throughout the entire domain. Local variation to τ^f near solid boundaries is the result of changes in the local concentration and orientation states.

The problem is non-dimensionalized by the fibre length L and the centreline fluid velocity u_{CL}, which result in the following dimensionless variables:

$$z = y/L, \quad \lambda = H/L, \quad U = u/u_{CL}, \quad \frac{\partial U}{\partial z} = \frac{L}{u_{CL}}\frac{\partial u}{\partial y},$$
$$Re = \frac{\rho u_{CL} L}{\mu}, \quad \overline{P} = \frac{P}{\rho u_{CL}^2}, \quad Pe_t = \frac{L u_{CL}}{D_t}, \quad Pe_r = \frac{u_{CL}}{L D_r},$$

where Pe_t and Pe_r are the translational and rotational Péclet numbers, respectively. The normalized concentration is defined as $\overline{n} = nL^3\eta(z)$, where $\eta(z)$ is used to characterize the variation in concentration across the channel and is defined such that $0 \leqslant \eta(z) \leqslant 1$.

2.1. *Flow evolution model*

The flow is described in the channel using Cauchy's momentum equations for a steady, quasi-one-dimensional, incompressible, Newtonian fluid, that is

$$\nabla \cdot \boldsymbol{U} = 0, \tag{2.2}$$

$$\boldsymbol{U} \cdot \nabla \boldsymbol{U} = -\nabla \overline{P} + \frac{1}{Re}\nabla \cdot \tau, \tag{2.3}$$

where $\boldsymbol{\tau}$ is the stress tensor, which is the sum of both the Newtonian fluid and fibre contributions

$$\boldsymbol{\tau} = \mu(\nabla \boldsymbol{U} + \nabla \boldsymbol{U}^{\mathrm{T}}) + \boldsymbol{\tau}^{fibre}. \tag{2.4}$$

The contribution from the fibre phase to the total stress in the suspension flow is given by (1.3). It depends on the local orientation and concentration state of the suspension which is described by the probability density function Ψ. The models for fibre concentration and orientation are described in the following sections.

2.2. *Fibre concentration model*

The dimensionless concentration distribution across the channel, $\overline{n}(\boldsymbol{r}, t)$, evolves according (1.15) where the migration velocity, v_{mig}, is modelled according to Ma & Graham (2005). Combining (1.3)–(1.7), (1.11), (1.12) and (1.15), integrating once with respect to z and applying the boundary condition given by (1.16) results in the non-dimensional model equations for the steady-state concentration distribution across the channel:

$$0 = \frac{1}{Pe_t}\frac{\partial \eta}{\partial z} + \frac{\widehat{K}(z)}{z^2}\eta + \frac{\widehat{K}(\lambda - z)}{(\lambda - z)^2}\eta \tag{2.5}$$

with boundary conditions

$$\eta(0) = 0, \tag{2.6}$$

$$\eta(\lambda/2) = 1, \tag{2.7}$$

where $\widehat{K}$ is defined as

$$\widehat{K} = \frac{u_{CL}}{L}K, \tag{2.8}$$

where

$$K(z) = \left(\frac{\pi \overline{n}\mu}{6\ln(2r)}Q(\epsilon) + A\frac{\pi \overline{n}^2 \mu}{3\ln^3(2r)}\right)\frac{\Delta(z)}{\overline{n}} \tag{2.9}$$

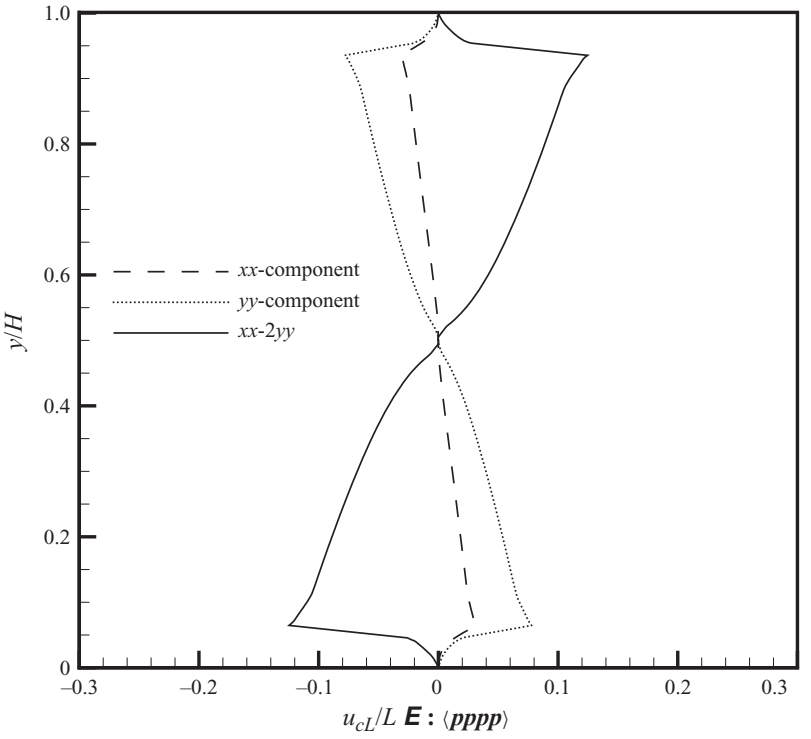

FIGURE 2. Variation of $\boldsymbol{E} : (\langle \boldsymbol{pppp} \rangle - \boldsymbol{I}\langle \boldsymbol{pp} \rangle)$ across the channel. The concentration shown here is $nL^3 = 10.8$.

and

$$\Delta = \boldsymbol{E} : (\langle \boldsymbol{pppp} \rangle - \boldsymbol{I}\langle \boldsymbol{pp} \rangle)_{11} - 2\boldsymbol{E} : (\langle \boldsymbol{pppp} \rangle - \boldsymbol{I}\langle \boldsymbol{pp} \rangle)_{22}. \tag{2.10}$$

Before a solution to (2.5) is given, it is instructive to present first an example of the $11/xx$, $22/yy$ components of $\boldsymbol{E} : (\langle \boldsymbol{pppp} \rangle - \boldsymbol{I}\langle \boldsymbol{pp} \rangle)$ along with $\Delta(z)$. These are plotted in figure 2. The exact solution to (2.5), based on the peak near-wall value of $\Delta(z = 0.5)$, is

$$\eta(z) = \frac{\dfrac{Q(\epsilon)}{6\ln(2r)} \exp\left(-\dfrac{Q(\epsilon)}{6\ln(2r)} L_d \left(\dfrac{1}{z} + \dfrac{1}{\lambda - z} - \dfrac{\lambda}{4} \right) \right)}{\dfrac{Q(\epsilon)}{6\ln(2r)} + \dfrac{A_{iso}}{3\ln^3(2r)} \left(1 - \exp\left(-\dfrac{Q(\epsilon)}{6\ln(2r)} L_d \left(\dfrac{1}{z} + \dfrac{1}{\lambda - z} - \dfrac{\lambda}{4} \right) \right) \right)} \tag{2.11}$$

where

$$L_d = \Delta_{wall} Pe_t \tag{2.12}$$

Nomenclature similar to that of Ma & Graham (2005) is used here, where their definition of L_d corresponds to the depletion layer thickness. This is not necessarily the case here, where we simply define the term L_d, i.e. (2.12), to obtain a less cumbersome closed form solution for $\overline{n}$ and one that more closely resembles that of Ma & Graham (2005). Furthermore, concentration-specific solutions are obtained using the peak, near-wall value of Δ, i.e. at $z = 0.5$, the one-half fibre length distance from the wall, and then fitting Pe_t such that the analytic solution matches the experimental measurements. We could have chosen an arbitrary value for Δ and

fitted Pe_t according to this arbitrary value. So, in essence, we are fitting the parameter L_d to the experimental measurements. However, we proceed by using Δ evaluated at the half fibre length distance from the wall in order to follow some systematic approach.

2.3. *Fibre orientation model*

An exact equation for ψ can be derived from (1.8) using the definition of Ψ. However, the resulting equation is highly nonlinear and particularly difficult, if not impossible to solve. Therefore, we use an approach similar to that of Ma & Graham (2005) and employ a traditional model of fibre orientation (e.g. Leal & Hinch 1971; Folgar & Tucker 1984; Altan *et al.* 1989; Koch 1995; Lin & Zhang 2002; Parsheh *et al.* 2005). For a fully developed flow in the x-direction, ψ evolves according to a Fokker–Planck equation, i.e.

$$\frac{1}{Pe_t}\frac{\partial^2\psi}{\partial z^2} = \frac{\partial(\dot{\phi}\psi)}{\partial\phi} - \frac{1}{Pe_r}\frac{\partial^2\psi}{\partial\phi^2}. \tag{2.13}$$

Olson *et al.* (2004) derived the following relationship for the angular velocity of the fibre in the xy-plane:

$$\dot{\phi} = -\frac{\partial U}{\partial z}\sin^2(\phi). \tag{2.14}$$

Equation (2.14) is general for a fibre rotating in a linear field and is identical to that derived by Jeffery (1922) for fibres of a large aspect ratio. Six boundary conditions are required in order to obtain an exact solution to (2.13). Since the ends of a fibre are indistinguishable, periodic boundary conditions are enforced with respect to the orientation angle, ϕ, i.e.

$$\psi(z,\phi) = \psi(z,\phi+\pi), \tag{2.15}$$

$$\frac{\partial\psi}{\partial\phi}(z,\phi) = \frac{\partial\psi}{\partial\phi}(z,\phi+\pi). \tag{2.16}$$

Since ψ is a distribution function, a third boundary condition stems from a normalization constraint (given a fibre is found at the point z), i.e.

$$\int_{\phi_1(z)}^{\phi_2(z)} \psi(z,\phi)\mathrm{d}\phi = 1, \tag{2.17}$$

$$\phi_1(z) = \begin{cases} -\pi/2, & z \geqslant 0.5,\ z \leqslant \lambda - 0.5, \\ \arcsin(z), & z \leqslant 0.5, \\ \arcsin(\lambda - z), & z \geqslant \lambda - 0.5, \end{cases} \tag{2.18}$$

$$\phi_2(z) = \begin{cases} \pi/2, & z \geqslant 0.5, \text{ and } z \leqslant \lambda - 0.5, \\ \arcsin(-z), & z \leqslant 0.5, \\ \arcsin(z - \lambda), & z \geqslant \lambda - 0.5. \end{cases} \tag{2.19}$$

The remaining four boundary conditions result from the no-flux condition on ψ near the channel walls. For the geometry and assumptions considered here, the no-flux condition at the channel walls is expressed as follows:

$$\frac{1}{Pe_t}\frac{\partial\psi}{\partial z} \pm \left(\dot{\phi}\psi - \frac{1}{Pe_r}\frac{\partial\psi}{\partial\phi}\right) = 0 \tag{2.20}$$

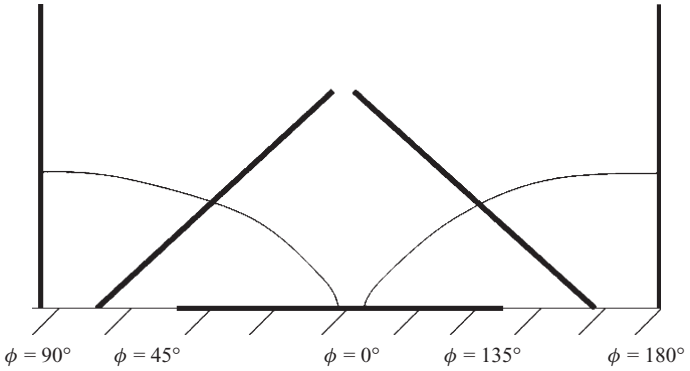

FIGURE 3. Coupling between translational and rotational motions at a solid boundary.

on $z = \pm 0.5 \sin \phi$, and

$$\frac{1}{Pe_t}\frac{\partial \psi}{\partial z} \mp \left(\dot{\phi}\psi - \frac{1}{Pe_r}\frac{\partial \psi}{\partial \phi}\right) = 0 \tag{2.21}$$

on $z = \lambda \mp 0.5 \sin \phi$

It should be pointed out that the migration velocity is not included in the near-wall boundary conditions for ψ since the relationship derived by Ma & Graham (2005), i.e. (1.11), represents an average over all orientation states. Therefore, it would not be sensible to include this term here, where there is a strong dependence on fibre orientation. To reiterate, the conditions defined by (2.20) and (2.21) state that for a fibre in contact with a wall, translational and rotational motions must be coupled in order to prevent a fibre from rotating or translating through the wall; see figure 3.

2.4. *Numerical implementation*

Numerical computations are carried out for the flow of semi-dilute fibre suspensions of concentration $nL^3 = 3.6$, 10.8 and 15.0. The channel geometry is shown in figure 1 where we use a channel height, $\lambda = 10$. On the basis of the measurements of Krochak, Martinez & Olson (2008), we set $Pe_r = 240$, 193 and 126, which values correspond to the concentrations $nL^3 = 3.6$, 10.8 and 15.0, respectively. Values of Pe_t are fitted to experimental measurements of the concentration distributions across the channel. Values of Pe_t were found to be 120, 180 and 1000, respectively.

The computational domain consists of a two-dimensional rectangular channel, 200 fibre lengths long and 10 fibre lengths in height. In the z-direction, we use a 200-point, uniform mesh of size $\Delta z = 0.05$, while in the x-direction, we use a uniform mesh of size $\Delta x = 2$, resulting in a 100×200 mesh in the spatial domain. A uniform, 500 point mesh is used to discretize the ϕ-domain. The flow field in the channel is computed using a commercial CFD software package, FLUENT (www.fluent.com). The solution to the flow field is obtained using a two-dimensional, segregated, implicit solver, with water at 20° C as the fluid phase. A no-slip condition is enforced along the channel walls. A parabolic velocity profile is assigned at the channel inlet with a Reynolds number, based on the peak velocity, $Re = 500$. Velocity field data used in solving (2.13) are extracted along a single, vertical slice far enough downstream of the inlet so that the flow is fully developed in the x-direction.

At distances greater than $L/2$ from the channel walls, (2.13) is discretized using second-order accurate, centred differences in both z and ϕ spaces. This yields the

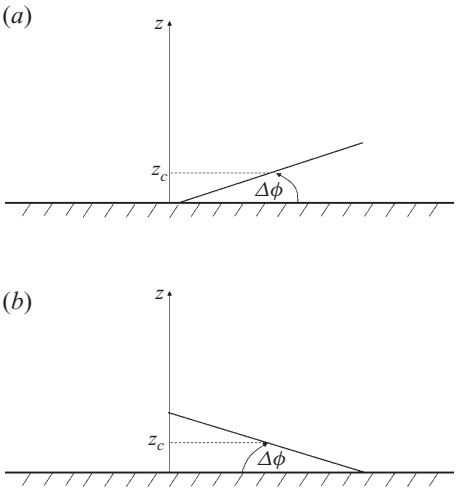

FIGURE 4. A schematic of the two possible fibre configurations along the lower wall. A fibre with (*a*) positive orientation at the wall and (*b*) negative orientation at the wall.

following system of equations to be solved at an arbitrary point, (ϕ_i, z_j), in the central part of the channel:

$$\frac{1}{Pe_t}\frac{\psi_{i,j+1}-2\psi_{i,j}+\psi_{i,j-1}}{\Delta z^2}=\frac{1}{Pe_r}\frac{\psi_{i+1,j}-2\psi_{i+1,j}+\psi_{i+1,j}}{\Delta\phi^2} - \dot{\phi}_{i,j}\frac{\psi_{i+1,j+1}-\psi_{i+1,j-1}}{2\Delta\phi}-\frac{\dot{\phi}}{\Delta\phi}_{i,j}\psi_{i+1,j}. \quad (2.22)$$

At the boundaries, specifically along the hypersurface separating the allowable from the forbidden orientation state, (2.20) and (2.21) are discretized using forward differences with respect to the wall-normal direction, both in position and in orientation. This results in four regions that must be handled separately, each corresponding to one of the two ends of a fibre touching either the top or bottom wall in the channel; see figure 4.

At the lower wall, the spatial derivative is defined using forward differences as follows:

$$\frac{\partial\psi}{\partial z}=\frac{\psi_{i,j+1}-\psi_{i,j}}{\Delta z}. \quad (2.23)$$

At the upper wall, the spatial derivative is defined using backward differences as follows:

$$\frac{\partial\psi}{\partial z}=\frac{\psi_{i,j}-\psi_{i,j-1}}{\Delta z}. \quad (2.24)$$

For a fibre in contact with the wall with positive orientation, the ϕ derivative is defined as follows:

$$\frac{\partial\psi}{\partial\phi}=\frac{\psi_{i,j}-\psi_{i-1,j}}{\Delta\phi}. \quad (2.25)$$

For a fibre in contact with the wall with negative orientation, the ϕ derivative is defined as follows:

$$\frac{\partial\psi}{\partial\phi}=\frac{\psi_{i+1,j}-\psi_{i,j}}{\Delta\phi}. \quad (2.26)$$

This yields the following system to be solved in the near-wall regions:

(*a*) Region 1. Lower wall, fibre oriented with positive ϕ

$$-\frac{1}{Pe_t}\frac{\psi_{i,j+1}-\psi_{i,j}}{\Delta z}+\left(\dot{\phi}_{i,j}\psi_{i,j}-\frac{1}{Pe_r}\frac{\psi_{i,j}-\psi_{i-1,j}}{\Delta\phi}\right)=0. \tag{2.27}$$

(*b*) Region 2. Lower wall, fibre oriented with negative ϕ

$$-\frac{1}{Pe_t}\frac{\psi_{i,j+1}-\psi_{i,j}}{\Delta z}+\left(\dot{\phi}_{i,j}\psi_{i,j}-\frac{1}{Pe_r}\frac{\psi_{i+1,j}-\psi_{i,j}}{\Delta\phi}\right)=0. \tag{2.28}$$

(*c*) Region 3. Upper wall, fibre oriented with positive ϕ

$$-\frac{1}{Pe_t}\frac{\psi_{i,j}-\psi_{i,j-1}}{\Delta z}+\left(\dot{\phi}_{i,j}\psi_{i,j}-\frac{1}{Pe_r}\frac{\psi_{i,j}-\psi_{i-1,j}}{\Delta\phi}\right)=0. \tag{2.29}$$

(*d*) Region 4. Upper wall, fibre oriented with negative ϕ

$$-\frac{1}{Pe_t}\frac{\psi_{i,j}-\psi_{i,j-1}}{\Delta z}+\left(\dot{\phi}_{i,j}\psi_{i,j}-\frac{1}{Pe_r}\frac{\psi_{i+1,j}-\psi_{i,j}}{\Delta\phi}\right). \tag{2.30}$$

The pseudo-code for implementing the boundary conditions is given as follows:

(*a*) Beginning at $z_i=0$, for increasing i, check if z_i is less than $1/2$ or greater than $\lambda-(1/2)$.

(*b*) If true, compute $\phi_1(z_i)$ and $\phi_2(z_i)$ and apply the one-sided difference boundary equation corresponding to the associated region.

(*c*) Pass over all other allowable ϕ_j according to (2.22).

(*d*) If (*a*) is false, solve (2.22) without boundary conditions.

With a uniform distribution, ψ is initialized, i.e. $\psi=1/\pi$ after which (2.13)–(2.21) are solved iteratively with a Gauss–Seidel method until the relative change in the solution on successive iterations is less than 10^{-6}.

In order to couple the momentum equations to the fibre orientation equations, an iterative procedure is used whereby the flow field is initially determined for the pure fluid, that is flow with no fibres, after which (2.13) and (2.14) are solved using the initial flow field data. The contribution of the fibre phase to the total stress on the fluid is defined by (1.3) and is computed upon solving the orientation equations for ψ. On the first iteration, a constant value for the concentration distribution $\overline{n}$ is assumed, specifically $\overline{n}=nL^3$. This is used as an initial estimate for τ^f, after which (2.5)–(2.10) are solved exactly to give the variation of $\overline{n}(z)$ across the channel, which is then used to better estimate $\tau^f(z)$ across the channel. Once computed, the gradient of the fibre stress is determined and then treated as a momentum source term in the fluid momentum equations. This source term is implemented in FLUENT by means of a user-defined function written in C. The fluid flow equations are then solved again to produce a new flow field. On each iteration, the flow field is deemed to be converged when the L_2 norm of the solution residual is less than 10^{-6}. The process is repeated until the change in the L_2 norm of the velocity vector between successive iterations is less than 10^{-6}. In general, a total of four iterations of each of the flow field equations, and of the orientation equations, were required to obtain a fully converged solution.

Mesh resolution studies were performed on the numerical scheme described above using $L=5\,\text{mm}$, $r=50$ and $nL^3=3.6$. In general, mesh refinement in the x-direction was not a concern for the numerical predictions because in all cases, the orientation equations were solved far enough downstream such that the flow field was fully developed. In order to evaluate numerical convergence of the orientation equations, we compare components of the fourth-order orientation tensor, as defined by (1.4), computed on three different uniform mesh resolutions summarized in table 1.

Mesh	Δx	Δz	$\Delta\phi$
50 × 100 × 100	0.02	0.1	0.0314
100 × 200 × 500	0.01	0.05	0.0063
100 × 400 × 500	0.01	0.025	0.0063

TABLE 1. Summary of meshes considered in the grid resolution study.

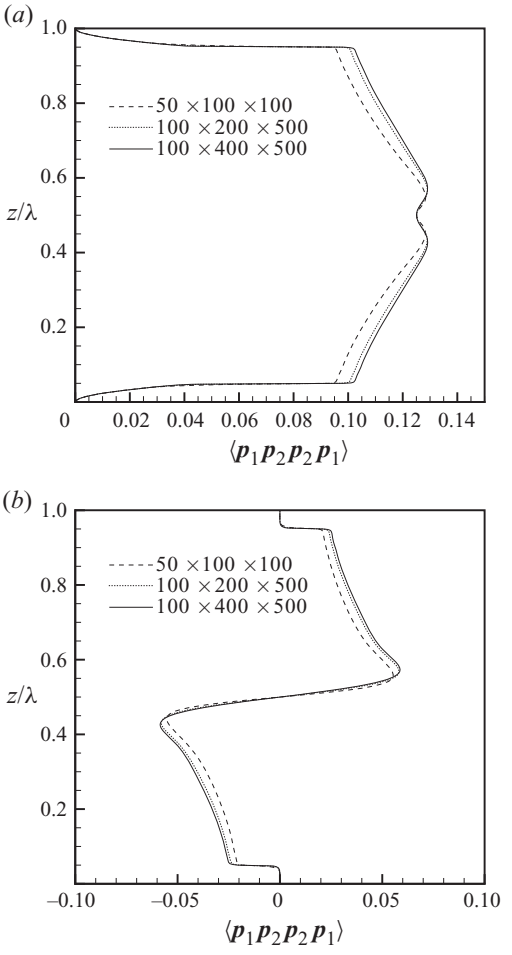

FIGURE 5. Comparison of the fourth-order orientation tensor components obtained with the three different mesh sizes: (*a*) $\langle \boldsymbol{p}_1\boldsymbol{p}_2\boldsymbol{p}_2\boldsymbol{p}_1\rangle$ and (*b*) $\langle \boldsymbol{p}_1\boldsymbol{p}_2\boldsymbol{p}_2\boldsymbol{p}_2\rangle$.

Specifically, we evaluate the components involved with the two-way, fluid/fibre coupling, i.e. $\langle \boldsymbol{p}_1\boldsymbol{p}_2\boldsymbol{p}_2\boldsymbol{p}_1\rangle$ and $\langle \boldsymbol{p}_2\boldsymbol{p}_2\boldsymbol{p}_2\boldsymbol{p}_2\rangle$; see figure 5.

In order to evaluate the numerical convergence of the fluid flow equations, we compare solutions obtained with the three spatial meshes described in table 1; see figure 6. Again, we see that the difference in solutions obtained on each mesh is extremely small.

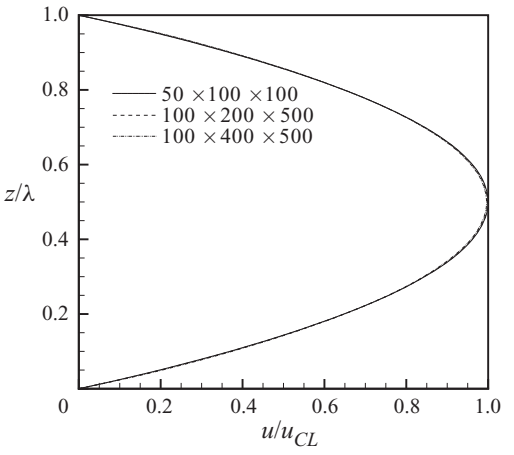

FIGURE 6. Comparison of the velocity profile obtained with the three different mesh sizes.

Although this analysis does not rigorously demonstrate the grid independence of our numerical predictions, figures 5 and 6 do show that variation with respect to the mesh sizes considered here is small. Therefore, we anticipate that our solution will not differ significantly if computed on a larger mesh. In particular, the difference between the finer two meshes is noticeably smaller than with the larger mesh. Given this result, and the necessary trade-off between accuracy and computational cost, all calculations and analysis that follow are made using the $100 \times 200 \times 500$ mesh.

3. Experimental procedures

An index-of-refraction matched suspension, that is a suspension consisting of fluid and fibre phases with identical indexes of refraction, is used to measure the orientation distribution function in an experimental channel. With this type of system, the fibre phase becomes indistinguishable from the fluid phase when observed under white light. A small number of fibres (less than 1 % of the total number of fibres) are then silvered and their motion is visualized in the flow using a digital camera in conjunction with an automated fibre-tracking programme. The motion and orientation of the observed fibres are assumed to represent the behaviour of all fibres within the suspension.

The experiments were performed in a rectangular cross-sectional Plexiglas cell of size $50 \times 255 \times 75$ mm (inlet height $\times$ length $\times$ width) proceeded by a hyperbolic contracting section used to stabilize the flow and remove any crossflow; see figure 7. Approximately 2.0 litre of suspension was required to fill the channel. Up- and downstream of the channel, reservoirs are set at different heights to control the pressure drop over the cell. The flow rate was set at $4.25 \times 10^{-5}\,\mathrm{m^3\,s^{-1}}$ using a gravity feed on the inlet side.

Borosilicate glass rods (www.mosci.com) of dimensions 5×0.1 mm (length $\times$ diameter) were employed as the fibre phase. The glass fibres had a density of approximately $2250\,\mathrm{kg\,m^{-3}}$. The index of refraction of these fibres was measured commercially and found to be 1.4719 ($\pm$0.0005). Approximately 0.01 % of the fibres in each suspension were silvered using Tollen's solution, a mixture of 5 ml of 0.1 M $AgNO_3$ with $\sim$ 10 µl (5 drops) of 0.4 M NaOH. Before silvering, the fibres were washed in detergent, rinsed in alcohol and then in distilled water. After silvering, the fibres were washed to remove any loosely adsorbed $AgNO_3$. We measured the

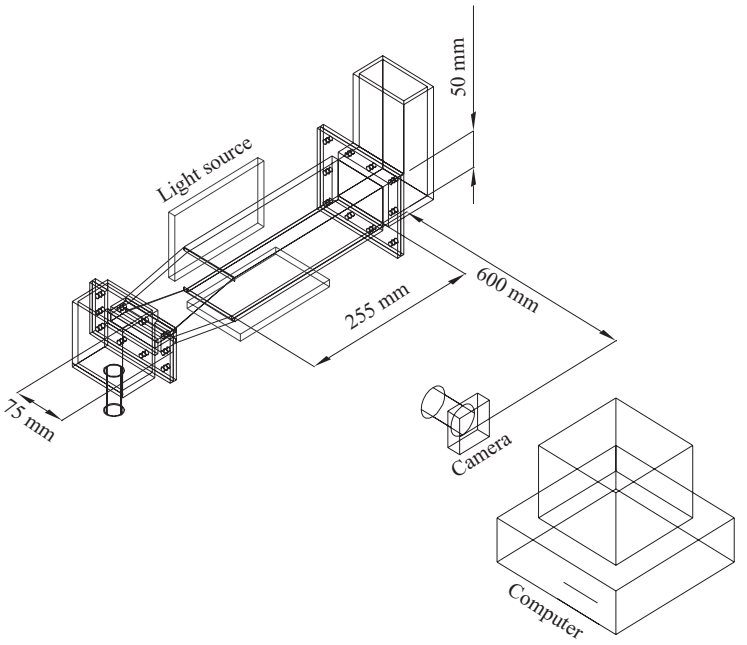

FIGURE 7. A schematic diagram of the experimental test section. Fibre orientation is observed immediately prior to the contracting section.

motion and orientation of three different monodispersed suspensions of concentration, $nL^3 = 3.6, 10.8$ and 15.0. Fibre orientation is observed immediately prior to the contracting section. The Newtonian fluid used in this system was glycerin with a density of 1260 kg m^{-3}, a viscosity of 1.49 Pa s and an index of refraction of 1.470. Fibre settling was not observed over the time scale of the experiment. Before each set of experiments, the suspension was stirred for several minutes using a variable frequency drive mixer (Midwest Mixing Corp.) until the fibres were uniformly distributed throughout the suspension.

Our visualization system consisted of a progressive scan Basler A201b monochrome CCD camera (10 bit grey scale and 1008×1016 pixel spatial resolution with a maximum framing rate of 30 frames per second), mounted with an F-mount Micro-NIKKOR 105 mm lens, positioned 60 cm in front of the observation section. The imaged area was 50×50 mm with a resolution of approximately 50 μm $pixel^{-1}$.

For particle tracking, the lens aperture and focus, backlight intensity and camera exposure time were chosen so that the whole imaged volume was within the depth of field of the lens. The camera was then re-focused in the middle of the xz-plane in an attempt to avoid measuring the orientation of fibres near the sidewalls. The Plexiglas cell was transilluminated using Schott–Fostec fibre optic dual backlight. The orientation of each particle was calculated using an in-house fibre tracking algorithm and consists of the following subroutines:

(*a*) *Particle identification.* Particle edges are detected using a Prewitt edge detection scheme with the original greyscale image converted to a binary image. Particle edge pixels are set to white (pixel value of 1) on a black background (pixel value 0). Particles are then dilated, the interior regions are filled with white pixels and then eroded back to their original size. The image now contains filled white particles on a black background. Any object whose length and width are less than 10 pixels in size,

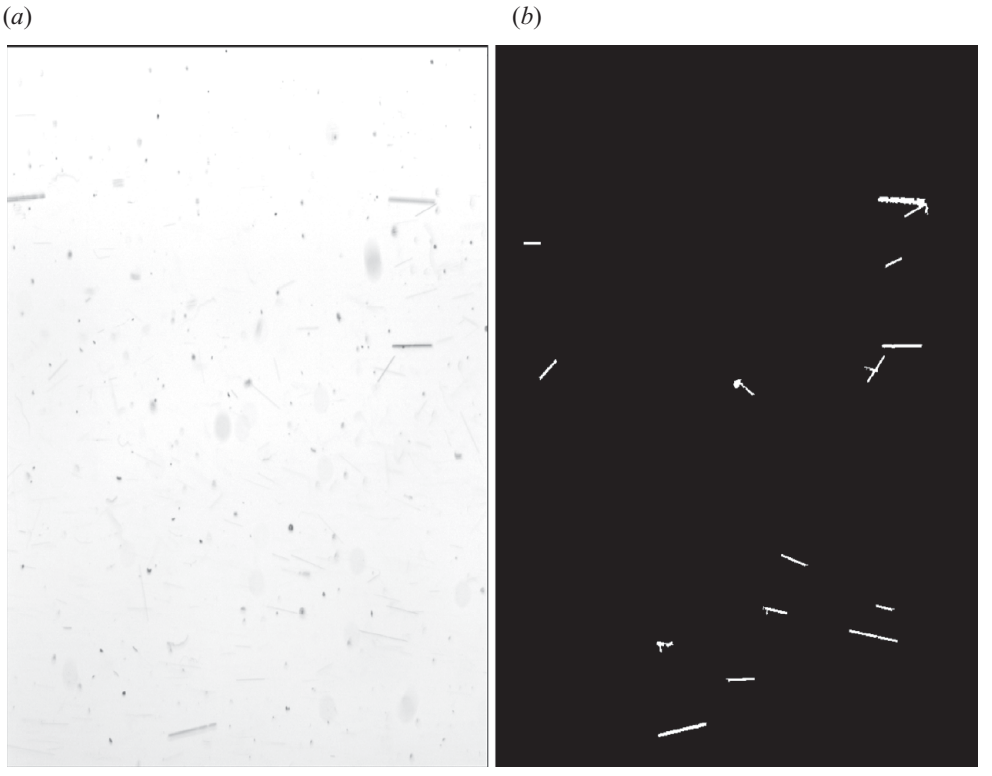

FIGURE 8. An example of (*a*) an original image and (*b*) a post-processed image with white fibres on a black background.

or whose length and width are approximately equal, are assumed to be artifacts in the image (e.g. air bubbles or non-fibrous debris) and are removed from the image. In addition, stationary objects were removed from the images.

(*b*) *Orientation distribution.* The orientation angle of each fibre is measured relative to the horizontal by computing the arctangent of the ratio $\Delta y/\Delta x$ between the end points of a fibre. The associated fibre length and centre of area are also recorded. The flow region is then partitioned into 5×5 mm cells and the orientation angle of each fibre whose centre of area lies within a particular cell is computed. There were on average approximately 5000 tracer fibre observations at each location for each experiment. Within each experimental cell, the distribution of fibre orientations was normalized to unity. The reason for choosing this form of normalization is discussed later.

Figure 8 shows an example of an original image and the same one after processing. Approximately 10 000 images were recorded for each set of fibre concentrations.

4. Results and discussion

In this section, numerical predictions of the orientation distribution function are compared with experimental observations across the channel gap. First, we present our results on the orientation state of the suspension in the near-wall region, i.e. the region less than $L/2$ from the channel walls. To reiterate, we argue that a rigorous formulation of the boundary conditions on ψ must be enforced in this region, and it will be shown that the no-flux boundary conditions described by (2.20) and (2.21)

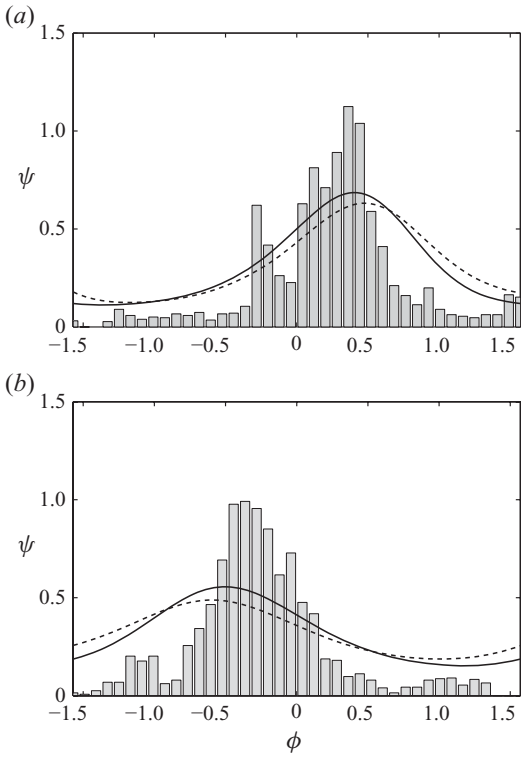

FIGURE 9. Comparison of the two-dimensional (solid line) and three-dimensional (dashed line) orientation distribution functions with experimental measurements. The corresponding channel positions are (*a*) $z = 2.5$ and (*b*) $z = 7.5$.

predict accurately the fibre orientation state in this region. A general orientation analysis will also be performed for distances greater than $L/2$ from the walls where all orientation states are physically possible and the system is well described by (2.13). We follow this with a comparison of the velocity profiles and the concentration profiles across the channel.

4.1. *Orientation distribution*

Before proceeding to the main findings of this section, we begin the analysis by investigating the assumption of a two-dimensional fibre orientation model. To reiterate, flow through the channel is assumed to be two-dimensional, and a planar model of fibre orientation is considered where each fibre is assumed to be oriented in the xy-plane with an orientation described by the single angle ϕ. While this is not true in theory as the rotary diffusion term creates out-of-plane orientation in planar flows, the character of the flow and orientation distribution will not be altered significantly, and we feel that the results from our predictions will still show the key phenomena in question. As a comparison, figure 9 shows the three-dimensional fibre orientation distribution alongside the two-dimensional orientation distribution in the absence of wall effects at two separate points in the channel, i.e. $z = 2.5$ and $z = 7.5$. Here, the planar orientation distribution function ψ^p is extracted from the three-dimensional orientation distribution function as follows:

$$\psi^p = \int_0^{\pi} \psi(\phi, \theta)\sin(\theta)\mathrm{d}\theta. \tag{4.1}$$

Figure 9 shows the main difference between the two-dimensional and three-dimensional orientation distributions, namely that the two-dimensional orientation distribution predicts a higher degree of alignment, i.e. the spread in the distribution is found to be smaller compared to the three-dimensional distribution function. This is explained by the fact that with the two-dimensional assumption, all of fibres are confined to the orientation plane, hence a greater number of fibres align in the principal direction of fibre orientation. The effect of the three-dimensional, out-of-plane distribution is to increase the spread in the planar orientation distribution. We do not feel that this small difference will significantly alter the character of the predictions presented below. Also shown in figure 9 is a comparison with the experimental measurements. The histogram of the orientation distribution function in both parts of the channel is found to be smooth and clustered around a definite value, namely $\phi \approx 0.3$ at $z \approx 2.5$ and $\phi = -0.3$ at $z = -2.5$. Here we also note a tendency for the model to overpredict the peak in the orientation distribution, i.e. the mean fibre orientation angle is predicted to be greater than is observed in the experiments.

We now turn our attention to the orientation distribution function at distances less than $L/2$ from the channel walls. Shown in figure 10 is a comparison of the numerical predictions with the experimental measurements. Here we compare results for $nL^3 = 3.6$; however, similar results were found for $nL^3 = 10.8$ and 15.0. The model agrees well with the experiments in this region, although it does overpredict fibre orientation closest to the wall. The most notable observation is that the model is able to capture the range of allowed orientation states in this region. Very close to the wall, specifically at distances $z \leqslant 0.1$, figures 10(a) and 10(b) show that nearly all fibres are aligned parallel to the wall, i.e. ψ is highly clustered about $\phi = 0$, a result which stems from the tight geometric constraint on fibre orientation in this region. Moving slightly farther away from the wall, but still in the region $z < (1/2)$, figure 10(c–e) shows that the peak in ψ begins to shift towards positive values in ϕ, while the spread in ψ begins to increase significantly. The increased spread in ψ indicates that fibres have more freedom to rotate in this region and therefore assume a greater range of orientations. However, the preferred direction of fibre orientation points away from the wall. The model agrees very well with the experiments in this region and does an excellent job of separating the allowed from the forbidden orientation states. Moving farther from the wall, figure 10(f) shows the point at which all orientation states are theoretically allowable, i.e. at the point $z = 1/2$. Here, the peak of ψ corresponds to a positive value in ϕ, which again indicates a tendency for fibres to point away from the wall. Furthermore, since fibre orientation is no longer restricted geometrically by the wall, and the spread in ψ encompasses all orientation states.

To fully characterize the fibre orientation distribution across the channel, we consider two measures of the orientation distribution function, namely the mean orientation angle, $\bar{\phi}$, and the orientation anisotropy, A_ϕ. The mean orientation angle corresponds to the principal direction of fibre alignment, i.e. the angle at which the majority of fibres are oriented. The orientation anisotropy corresponds to the degree of fibre alignment about the principal direction of orientation. As a reference, a value of A_ϕ equal to unity corresponds to a perfectly aligned suspension, e.g. $\psi = \delta(\phi - \phi_0)$, where δ is the Dirac delta-function. Conversely, a value of $A_\phi = 0.5$ corresponds to a suspension that is in a fully random, or uniform orientation state, e.g. $\psi = 1/\pi$. The terms $\bar{\phi}$ and A_ϕ are defined, respectively, as follows:

$$\bar{\phi} = \int_{-(\pi/2)}^{\pi/2} \phi \; \psi(z, \phi) \mathrm{d}\phi \tag{4.2}$$

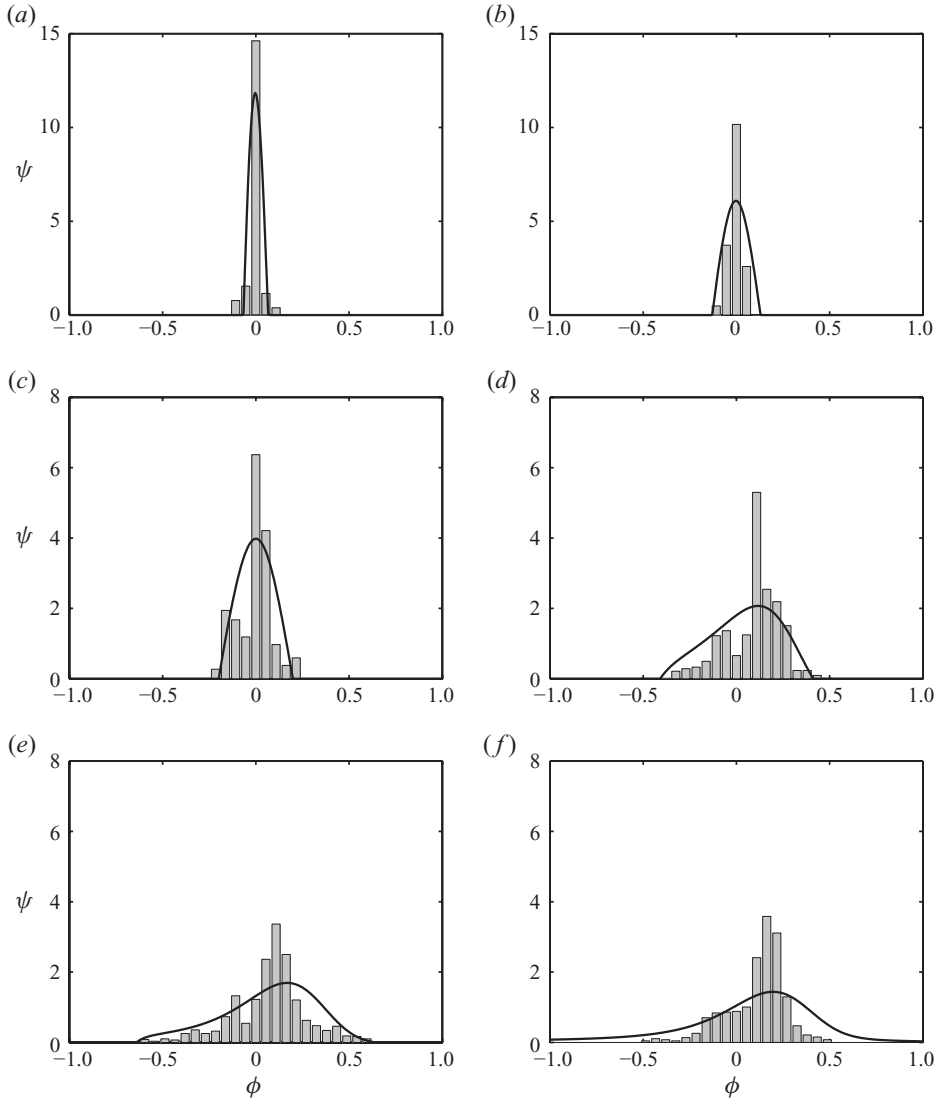

FIGURE 10. The orientation distribution at various distances in the near-wall region. (*a*) $y/L \to 0$, (*b*) $z = 0.1$ ($y/H = 0.01$), (*c*) $z = 0.2$ ($y/H = 0.02$), (*d*) $z = 0.3$ ($y/H = 0.03$), (*e*) $z = 0.4$ ($y/H = 0.04$), (*f*) $z = 0.5$ ($y/H = 0.05$). The concentration shown here is $nL^3 = 3.6$, the fibre length is 5 mm and the aspect ratio is 50.

and

$$A_\phi = \int_{-(\pi/2)}^{\pi/2} \cos^2\phi \; \psi(z, \phi) \mathrm{d}\phi. \tag{4.3}$$

Figure 11 compares a prediction of the profile of $\bar{\phi}$ with experimental measurements, where the error bars indicate the 95 % confidence interval. The concentration shown here is $nL^3 = 15.0$; however, similar results were found for $nL^3 = 3.6$ and 10.8. Here we see that in the lower half of the channel where $z \geqslant 0.5$, the mean direction of fibre alignment is positive, i.e. fibres in the lower half channel tend to point away from the lower wall towards the upper wall. Similarly, in the upper half channel

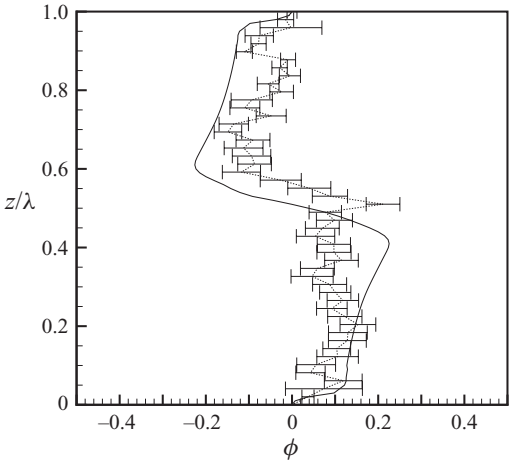

FIGURE 11. Comparison of the mean orientation angle across the channel. The model predictions are shown along with the experimental observations for $nL^3 = 15.0$. The error bars indicate the 95 % confidence interval.

where $z \leqslant \lambda - 0.5$, the mean direction of fibre alignment is negative, i.e. fibres in this region point away from the upper wall and towards the lower wall. These findings are due to the fact that fibre alignment is predominantly driven by local velocity gradients. In the lower half channel, the velocity gradient, $\partial u/\partial y$, is positive and fibres tend to align in the positive direction. Similarly, in the upper half channel, the velocity gradient is negative and fibres are aligned in the negative direction. Along the centreline, the mean fibre orientation is at $\phi = 0$, or parallel to the x-axis. At distances less than $L/2$, the mean fibre orientation angle increases from $\bar{\phi} = 0$ closest to the wall, to $\bar{\phi} \approx 0.1$ rad at $z = 0.5$. Excellent agreement is found between the model predictions and the experimental measurements in the near-wall region. Considerable discrepancies are apparent outside of this near-wall region. These discrepancies will be discussed below.

Figure 12 compares profiles of $\bar{\phi}$ predicted with and without the rigorous near-wall treatment of ψ along with the experimental measurements, in the near-wall region. Here, the effect of ignoring the rigorous boundary conditions on ψ results in an overprediction of $\bar{\phi}$ near the walls. Non-physical values of $\bar{\phi}$ are predicted at distances less than $L/2$ from the wall. However, this problem is corrected when a rigorous near-wall treatment is considered in the model.

Profiles of A_ϕ are compared in figure 13, where the error bars indicate the 95 % confidence interval. The model is able to give a good qualitative prediction of the character of A_ϕ across the channel. Specifically, A_ϕ is at a maximum closest to the channel walls where it tends towards a value of 1, indicating that all fibres in this region are aligned parallel to the walls. Note that A_ϕ then decreases nonlinearly to a minimum value at the centre of the channel where the suspension is at its most random in orientation. The cusp in the profiles indicates the $L/2$ distance from the wall. This finding reinforces the notion that the wall increases fibre alignment in the near-wall region. This result agrees well with the experimental findings of Moses *et al.* (2001) and Stover & Cohen (1990), where the wall was said to have a stabilizing effect of fibre orientation at distances less than $L/2$. Close to the walls, the model agrees quantitatively and qualitatively with the experimental observations. However, away from the walls, the model only agrees in character and quantitative agreement is not

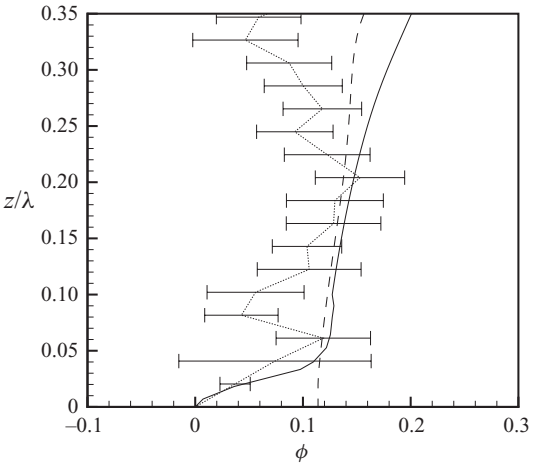

FIGURE 12. Comparison of the mean orientation angle close to the channel wall. The model predictions shown are computed with (—) and without (- - -) the wall boundary formulations along with the experimental observations. The concentration shown here is $nL^3 = 15.0$.

as strong. The quantitative ambiguities can most likely be accounted for by the fact that we have assumed a planar orientation of fibres in the numerical model, i.e. fibre alignment is assumed to be entirely in the xy-plane. However, in the experiments, fibre alignment is not limited to the xy-plane, and fibres are free to rotate in the out-of-plane direction. This is most certainly one major source of error.

The effect of increasing the fibre concentration appears as a reduction in A_ϕ across the channel, particularly along the channel centreline. This result is due to the fact that increasing the fibre concentration effectively increases the rotary diffusivity caused by the fibre–fibre interactions. More specifically, with a greater number of fibres confined to the same domain, the frequency of fibre–fibre interactions is increased and the suspension tends towards a more random orientation state. This observation has been previously reported by a number of different researchers (e.g. Stover, Koch, & Cohen 1992; Rahnama *et al.* 1995*b*; Rahnama, Koch & Cohen 1995*a*; Krochak*et al.* 2008). The model also predicts an increase in A_ϕ as the concentration is increased; however, this is expected since Pe_r decreased with increase in fibre concentration, i.e. D_r increases. It is interesting to note that the quantitative agreement between the numerical predictions and the experimental measurements tends to improve as the fibre concentration increases. This observation can be made for both $\bar{\phi}$ and A_ϕ. At this point, the reader may also be questioning the strange, yet persistent oscillations observed in both the plots of ϕ and A_ϕ. This issue will be discussed below; however, it is important to first investigate the velocity distribution in the channel.

4.2. *Velocity profiles*

In this section, we present numerical estimates of the two-dimensional velocity distribution arising from the suspension flow through the rectangular channel. Here we show that by including the rigorous formulation of the near-wall effects on the distribution function, we are able to improve the accuracy of the numerical predictions significantly. We do so by comparing our estimates of the velocity profiles in the channel with the experimental measurements of Xu & Aidun (2005). To reiterate, we assign a parabolic velocity distribution at the channel inlet and allow the suspension to evolve along the length of the channel where the fibre stress term, i.e. (1.3), is

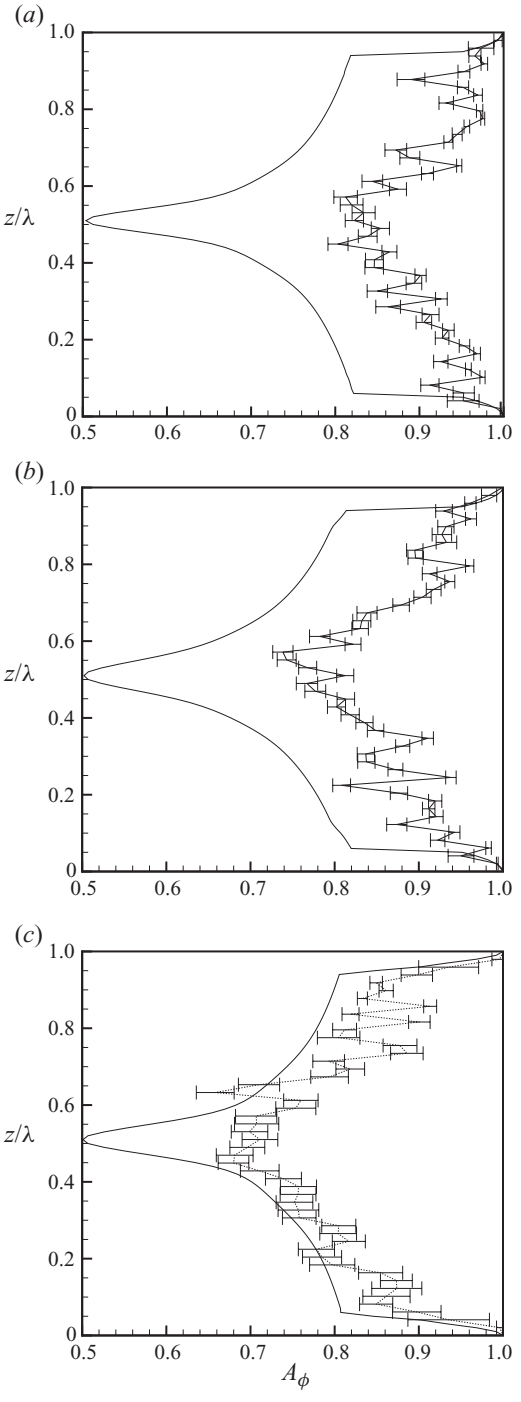

FIGURE 13. Comparison of the orientation anisotropy across the channel. The model predictions are shown along with the experimental observations for (*a*) $nL^3 = 3.6$, (*b*) $nL^3 = 10.8$ and (*c*) $nL^3 = 15.0$. The error bars indicate the 95 % confidence interval.

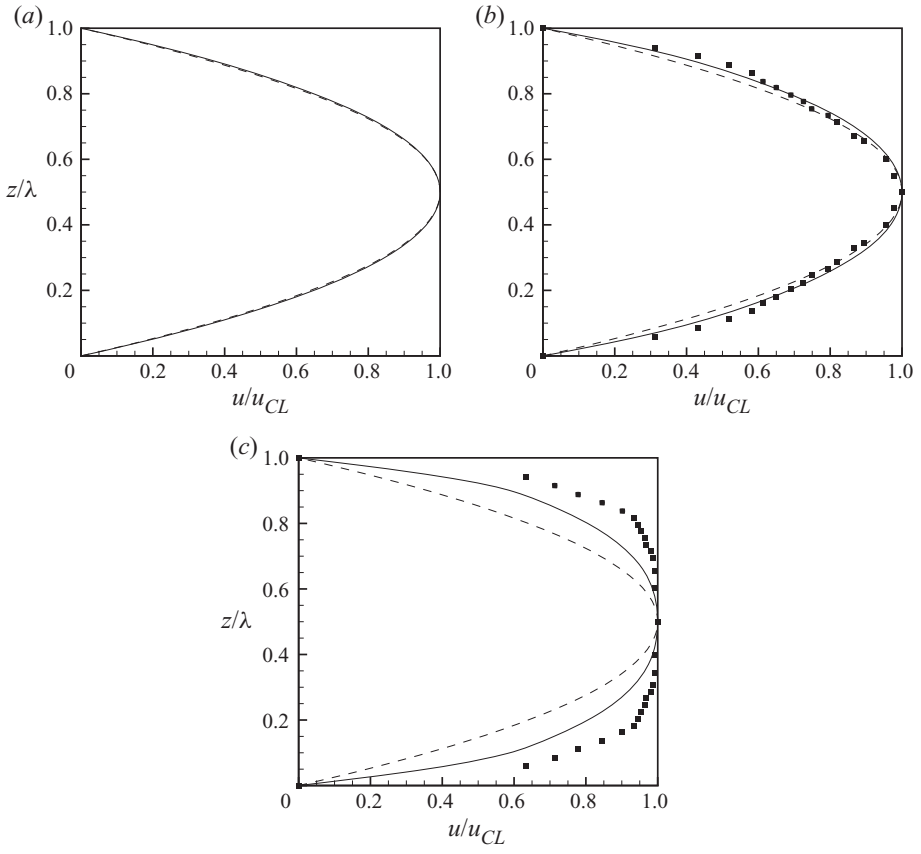

FIGURE 14. Comparison of the predicted velocity profiles with experimental measurements of Xu & Aidun (2005). The concentrations (numerical/experimental) shown here are (*a*) $nL^3 = 0/3.6$, (*b*) $nL^3 = 8/10.8$ and (*c*) $nL^3 = 16/15$. The squares (□) represent the experimental measurements of Xu & Aidun (2005), the solid lines (—) indicate the numerical predictions and the dotted lines (···) indicate a Newtonian fluid without fibres.

included in the flow equations. The predicted velocity profiles are then extracted far enough downstream such that the suspension has reached a fully developed state. It should be pointed out that the concentration measured by Xu & Aidun (2005) are not identical to those estimated by our calculations. However, the difference in concentrations is small, and we feel that it is worth making this comparison.

Figure 14 shows that by implementing the rigorous near-wall treatment of ψ and $\overline{n}$, we are better able to predict the velocity profile in the channel. The improvement is not significant for the lowest concentration, $nL^3 = 4$. As seen in figure 14(*a*), the fibres have almost no effect on the velocity profile. In this plot, we do not compare with any experimental measurements because none were available at such a low concentration. At $nL^3 = 10.8$, we see that the velocity gradient close to the wall has increased; see figure 14(*b*). Our calculations also show this increase in the velocity gradient close to the wall. Near the channel centreline, the velocity profile coincides with that of a Newtonian fluid, i.e. parabolic. At the highest concentration, i.e. $nL^3 \geqslant 15$, we see a significant change in the character of the velocity profile; see figure 14(*c*). Specifically, the velocity gradient near the wall has increased considerably and a plug-like region has formed away from the walls. Of course, it is clear that the model underpredicts

both the size of the plug region and the magnitude of the near-wall velocity gradients. The discrepancies found between the predicted and measured velocity profiles most likely stem from two major factors. The first is that we are comparing predictions based on a two-dimensional model of fibre orientation with measurements in which fibres have three-dimensional orientation. The second probable cause for the discrepancy is that the fibres used in the experiments of Xu & Aidun were flexible. This may lead to the formation of coherent, mechanically entangled flocs; see for example Martinez *et al.* (2001). In spite of this, we do see an improvement in the numerical predictions of the velocity distribution when the wall effects are considered in the model.

We are now in a position to comment on the oscillations that appear in the measurements of both $\bar{\phi}$ and A_ϕ across the channel. This is believed to be an indication that fibres are beginning to flocculate despite the fact that the fibre concentration is below the flocculation limit of $nL^3 = 32$ (e.g. Martinez *et al.* 2001; Krochak*et al.* 2008). We put forth the argument that fibres are segregating into small flocs, where the orientation state of each floc may differ slightly from that of neighbouring flocs. This argument can be supported by the velocity profiles of the flowing suspension. In particular, one important consequence of the formation of a plug region is that the velocity gradients vanish almost completely in this region along with any fibre alignment mechanism. Therefore, the behaviour of fibres in this region is determined entirely by the hydrodynamic fibre–fibre interactions, which may increase the likelihood of fibre flocculation.

4.3. *Concentration distribution*

We now compare concentration profiles in the suspension flow across the channel. In the experiments, it is assumed that the number of observed tracer fibres at an observation point is indicative of the fibre concentration at that point. In the theory, the normalized concentration distribution, $\eta(z)$, is defined by (2.11), where concentration-dependent values of Pe_t are fitted to the experimental data. Values of Pe_t and L_d (based on the peak near-wall fibre stress) were found to be $0.83\ldots, 0.55\ldots, 0.1000$ and $L_d = 5.38 \times 10^{-6}$, $5.97 \times 10^{-6}, 8.2 \times 10^{-6}$ for the bulk concentrations $nL^3 = 3.6, 10.8$ and 15.0, respectively. It should stressed that these values are fitting parameters that allow obtaining an exact solution to (2.5). A comparison of the predicted and experimentally observed concentration profiles is shown in figure 15. A conservation condition is applied on both the theoretical and experimental concentration distributions. Specifically, the concentration distributions are renormalized such that the integral of the concentration distribution across the channel equals the total number of expected fibres divided by nL^3. Schiek & Shaqfeh (1995) show that this normalization condition can be expressed mathematically as follows:

$$\frac{1}{nL^3}\int_0^\lambda \overline{n}(z)\,\mathrm{d}z = \lambda \tag{4.4}$$

or simply

$$\int_0^\lambda \eta(z)\,\mathrm{d}z = \lambda. \tag{4.5}$$

Two general trends are shown in figure 15. Specifically, as the concentration increases, the size of the depletion region decreases and the concentration profile becomes increasingly constant. That is, the fibres in the low concentration suspension tend to migrate towards the middle of the channel, while the concentration distribution becomes more and more uniform with increasing concentration. This phenomenon

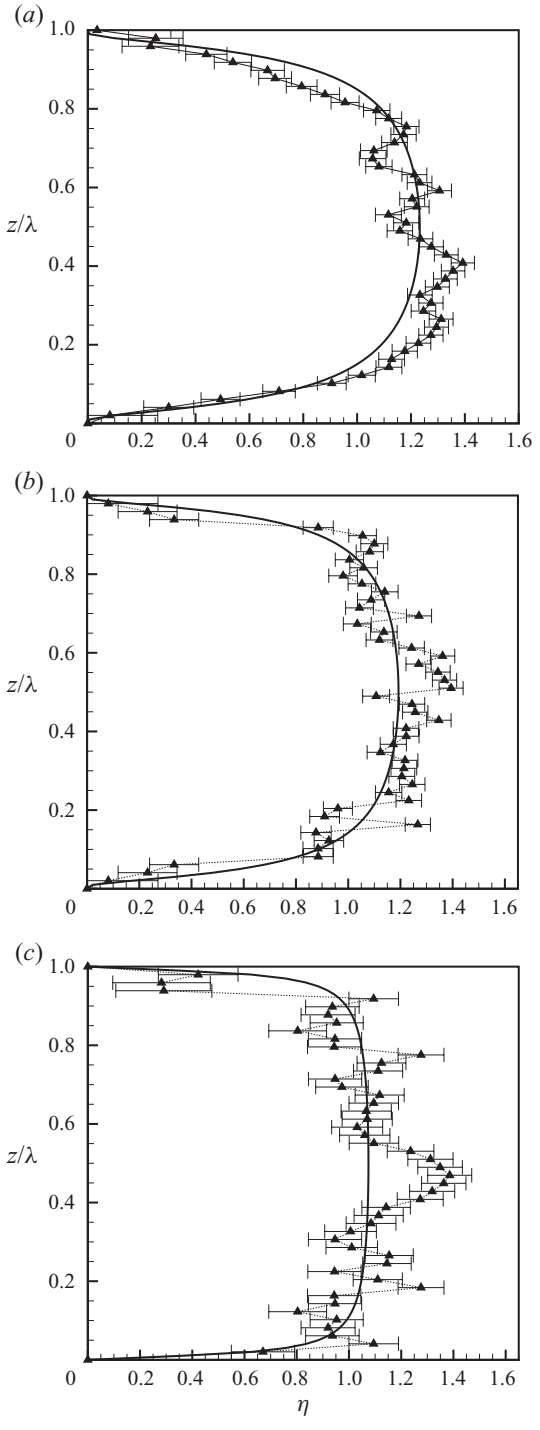

FIGURE 15. A comparison of the predicted and measured concentration profiles across the channel. The model predictions are shown as (—) along with the experimental observations (▲): (*a*) $nL^3 = 3.6$, (*b*) $nL^3 = 10.8$ and (*c*) $nL^3 = 15.0$.

supports the fibre migration theory that states that fibres migrate from regions of high to low shear stresses (e.g. Leighton & Acrivos 1987; Phillips *et al.* 1992; Ma & Graham 2005. An inspection of the velocity profiles, i.e. figure 14, shows that as the concentration increases, the velocity profile changes from parabolic to plug-like. For the parabolic velocity profile, the lowest shear stress occurs exactly along the centreline; hence, fibre concentration is greatest along the centreline. However, as the concentration increases, the shear stress in the central part of the channel decreases and fibre migration is reduced significantly. The reader will also notice the rather large oscillations in the experimental concentration distributions. These oscillations are similar to those observed in the profiles of $\bar{\phi}$ and A_ϕ and, here too, are an indication that fibres are beginning to flocculate. In fact, it is believed that the oscillations observed in the fibre concentration profiles support the argument that fibres are flocculating.

There are still a number of discrepancies between the model predictions and the experimental measurements, most notably, the model overpredicts $\bar{\phi}$ and A_ϕ away from the channel walls. This is likely to be due to the fact that, in this work, we have considered a two-dimensional model of fibre orientation. However, in the experiments, the fibres have three-dimensional orientation and are not limited to rotate solely in the xy-plane. While three-dimensional fibre orientation should not change the character of the fibre behaviour, it will certainly affect quantitative values of both $\bar{\phi}$ and A_ϕ. One possible cause for discrepancies in the near-wall region may be explained by the flipping fibre phenomenon, and the frequency of fibre flipping in relation to the suspension concentration. More specifically, for the lower concentration suspension, fibres entering the near-wall region were observed to flip by 180° (or several multiples thereof), more often compared to the higher concentration suspension. At the low concentration, these flipping fibres were observed to eventually drift to a distance well in excess of $L/2$ from the wall, after which they assumed a stable fibre orientation. At the higher concentration, not only were there far fewer occurrences of flipping fibres, but those which did flip, often remained much closer to the wall upon stabilizing, i.e. approximately $L/2$ from the wall. Similar observations have also been made by Stover & Cohen (1990) and Moses *et al.* (2001); however, here we find that at low concentrations, fibres drift out to distances on the order L after undergoing this pole-vaulting action, whereas Stover & Cohen (1990) and Moses *et al.* (2001) found that fibres drifted to a distance of approximately $L/2$ from the wall, even in the dilute limit. Another possible explanation for this observation is that, at low concentrations, fibres have fewer neighbours so that flipping fibres are less likely to mechanically interact with other fibres, allowing them the freedom to drift farther away from the walls. Capturing such detailed fibre behaviour is one inherent deficiency with the Eulerian approach to fibre suspension modelling. Nonetheless, the Eulerian model used here is able to predict these linear concentration profiles, which could arguably result from the flipping fibre phenomenon.

5. Conclusion

A numerical model has been presented to predict the orientation and concentration states of rigid fibre suspensions in a rectangular channel flow. A rigorous formulation of the wall boundary conditions has been implemented in the model, allowing accurate predictions of fibre orientation across the entire channel and up to the channel walls. Hydrodynamic fibre–wall interactions have also been considered causing fibres to migrate from regions of high to low shear stresses. Measurements of fibre orientation

and concentration were carried out in an experimental device in order to validate the model. Good qualitative agreement was found between the model predictions and the experimental measurements across the entire channel. The model agreed particularly well in the near-wall region, both qualitatively and quantitatively. Away from the channel walls, good qualitative agreement was shown with the quantitative discrepancies being attributed to flocculation and to our neglecting the out-of-plane fibre orientation in the numerical model.

Estimates of the velocity distributions of fibre suspension flow through the channel have been made using a two-way coupled model of the suspension flow, and predictions made with a rigorous treatment of near-wall interactions are compared to the experimental measurements of Xu & Aidun (2005). It has been shown that by considering both the rigorous no-flux boundary conditions on the orientation distribution function, along with hydrodynamic wall interactions for the concentration distribution, significant improvements can be made to estimates of the velocity profile. It is further argued that shortcomings of the model stem from fibre flocculation and mechanical entanglement, two phenomena that cannot be described with the model presented here.

Concentration measurements have been made in the channel using an index-of-refraction matched suspension. Both the predicted and measured concentration profiles clearly showed a nonlinear increase in fibre concentration from the channel wall, reaching a maximum value near the centre of the channel. At low concentration, a clearly defined maximum in concentration was found along the channel centreline. As the concentration increased, the concentration distribution became increasingly uniform across the channel and the size of the depletion zone decreased significantly. Good agreement was shown between the model predictions and the experimental measurements.

REFERENCES

Agarwal, U. S., Dutta, A. & Mashelkar, R. A. 1994 Migration of macromolecules under flow: the physical origin and engineering implications. *Chem. Engng Sci.* **49**, 1693–1717.

Altan, M. C., Advani, S. G., Güceri, S. I. & Pipes, R. B. 1989 On the description of the orientation state for fibre suspensions in homogeneous flows. *J. Rheol.* **33**, 1129–1155.

Anczurowski, E. & Mason, S. G. 1968 Particle motions in sheared suspensions: rotation of rigid spheroids and cylinders. *Trans. Soc. Rheol.* **12**, 209–215.

Batchelor, G. K. 1970 Slender-body theory for particles of arbitrary cross-section in Stokes flow. *J. Fluid Mech.* **44**, 419–440.

Batchelor, G. K. 1971 The stress generated in a non-dilute suspension of elongated particles by pure straining motion. *J. Fluid Mech.* **46**, 813–829.

Bibbo, M. A., Dinh, S. M. & Armstrong, R. C. 1985 Shear flow properties of semi-concentrated fibre suspension. *J. Rheol.* **29** (6), 905–929.

Bretherton, F. P. 1962 The motion of rigid particles in a shear flow at low Reynolds number. *J. Fluid Mech.* **14**, 284–304.

Cox, R. G. 1970 The motion of long slender bodies in a viscous fluid. *J. Fluid Mech.* **44**, 791–810.

Dinh, S. M. & Armstrong, R. C. 1984 A Rheological equation of state for semi-concentrated fibre suspensions. *J. Rheol.* **28** (3), 207–227.

Folgar, F. 1983 Orientation behaviour of fibres in concentrated suspensions. PhD thesis, University of Illinois at Urbana-Champaign, Illinois.

Folgar, F. & Tucker, C. L. 1984 Orientation behaviour of fibres in concentrated suspensions. *J. Reinf. Plast. Comp.* **3**, 98–119.

Forgacs, O. L., Robertson, A. A. & Mason, S. G. 1958 The hydrodynamic behaviour of paper-making fibers. *Pulp Paper Mag. Canada* **59**, 117–127.

Gillissen, J., Boersma, B., Mortensen, P. & Andersson, H. 2007 The stress generated by non-Brownian fibres in turbulent channel flow simulations. *Phys. Fluids* **19**, 115107.

Goldsmith, H. L. & Mason, S. G. 1962 The flow of suspension through tubes. Part I. Single spheres. *J. Colloid. Sci.* **17**, 448–476.

Heath H. S., Olson, J. A., Buckley, K. R., Lapi, S., Ruth, T. J. & Martinez, D. M. 2007 Visualization of the flow of a fibre suspension through a sudden expansion using PET. *AIChE J.* **53**, 327–334.

Jefferey, G. B. 1922 The motion of ellipsoidal particles immersed in a viscous fluid. *Proc. R. Soc. Lond.* A **102**, 161–179.

Kim, S. 1986 Singularity solutions for ellipsoids in low-Reynolds-number flows: with applications to the calculation of hydrodynamic interactions in suspensions of ellipsoids. *Intl J. Multiphase Flow* **12**, 469–491.

Koch, D. L. 1995 A model for orientational diffusion in fibre suspensions. *Phys. Fluids* **7** (8), 2086–2088.

Krochak, P. J., Martinez, D. M. & Olson, J. A. 2008 The orientation of semi-dilute rigid fibre suspensions in a linearly contracting channel. *Phys. Fluids* **20**, 073303.

Leal, L. G. & Hinch, E. J. 1971 The effect of weak Brownian rotations on particles in shear flow. *Chem. Engng Comm.* **108**, 381–401.

Leighton, D. & Acrivos, A. 1987 The shear-induced migration of particles in concentrated suspensions. *J. Fluid Mech.* **181**, 415–439.

Lin, J. & Zhang, L. 2002 Numerical simulation of orientation distribution function of cylindrical particle suspensions. *Appl. Math. Mech.* **23**, 906–912.

Lipscomb, G. G. & Denn, M. M. 1988 Flow of fibre suspensions in complex geometries. *J. Non Newtonian Fluid Mech.* **26**, 297–325.

Ma, H. & Graham, M. D. 2005 Theory of shear induced migration in dilute polymer solutions near solid boundaries. *Phys. Fluids* **17**, 083103.

Mackaplow, M. B. & Shaqfeh, E. S. G. 1996 A numerical study of the rheological properties of suspensions of rigid, non-Brownian fibers. *J. Fluid Mech.* **329**, 155–186.

Martinez, D. M., Buckley, K., Linstrom, A., Thiruvengadaswamy, R., Olson, J. A., Ruth, T. J. & Kerekes, R. J. 2001 Characterizing the mobility of papermaking fibres during sedimentation. In *Proceedings of the Twelfth Fundamental Research Symposium*, Oxford, pp. 225–254. The Pulp and Paper Fundamental Research Society, Lancashire, UK.

Moses, K. B., Advani, G. S. & Reinhardt, A. 2001 Investigation of fibre motion near solid boundaries in simple shear flow. *Rheol. Acta* **40**, 296–306.

Nitsche, J. M. & Roy, P. 1996 Shear-induced alignment of nonspherical Brownian particles near wall. *AIChE J.* **42**, 2729–2742.

Nitsche, L. C. & Hinch, E. J. 1997 Shear-induced lateral migration of Brownian rigid rods in parabolic channel flow. *J. Fluid Mech.* **332**, 1–21.

Olson, J. A., Frigaard, I., Chan, C. & Hämäläinen, J. P. 2004 Modeling a turbulent fibre suspension flowing in a planar contraction: the one-dimensional headbox. *Intl J. Multiphase Flow* **30**, 51–66.

Parsheh, M., Brown, M. L. & Aidun, C. K. 2005 On the orientation of stiff fibres suspended in a turbulent flow in a planar contraction. *J. Fluid Mech.* **545**, 245–269.

Paschkewitz, J. S., Yves, D., Dimitropoulos, C. D., Shaqfeh, E. S. & Parviz, M. 2004 Numerical simulation of turbulent drag reduction using rigid fibers. *J. Fluid Mech.* **518**, 281–317.

Phelps, J. H., Tucker, C. L. 2009 An anisotropic rotary diffusion model for fibre orientation in short and long-fibre thermoplastics. *J. Non Newtonian Fluid Mech.* **156**, 165–176.

Phillips, R. J., Armstrong, R. C., Brown, R. A., Graham, A. L. & Abbott, J. R. 1992 A constitutive equation for concentrated suspensions that accounts for shear induced particle migration. *Phys. Fluids* A **4**, 30–40.

Rahnama, M., Koch, D. L., Iso, Y. & Cohen, C. 1993 Hydrodynamic, translational diffusion in fibre suspensions subject to simple shear-flow. *Phys. Fluids* A **5**, 849–862.

Rahnama, M., Koch, D. L. & Cohen, C. 1995*a* Observations of fibre orientation in suspensions subject to planar extensional. flows. *Phys. Fluids* **7**, 1811–1817.

Rahnama, M., Koch, D. L. & Shaqfeh, E. S. G. 1995*b* The effect of hydrodynamic interactions on the orientation distribution in a fibre suspension subject to simple shear flow. *Phys. Fluids* **7**, 487–506.

Ranganathan, S. & Advani, S. G. 1991 Fiber–fibre interactions in homogeneous flows of nondilute suspensions. *J. Rheol.* **35**, 1499–1522.

Schiek R. L. & Shaqfeh, E. S. G. 1995 A non-local theory for stress in bound, Brownian suspensions of slender, rigid fibers. *J. Fluid Mech.* **296**, 271–324.

Stover, C. A. 1991 The dynamics of fibres suspended in shear flows. PhD thesis, School of Chemical Engineering, Cornell University, Ithaca, New York.

Stover, C. A. & Cohen, C. 1990 The motion of Rodlike particles in the pressure-driven flow between two flat plates. *Rheol. Acta* **29**, 192–203.

Stover, C. A., Koch, D. L. & Cohen, C. 1992 Observation of fibre orientations in simple shear flow of semi dilute suspensions. *J. Fluid Mech.* **238**, 277–296.

VerWeyst, B. E. & Tucker, C. L. 2002 Fiber suspensions in complex geometries: flow/fibre coupling. *Can. J. Chem. Engng* **80**, 1093–1106.

Xu, H. J. & Aidun, C. K. 2005 Characteristics of fibre suspension flow in a rectangular channel. *Intl J. Multiphase Flow* **31**, 318–386.